

A11102 484894

REFERENCE

NBS
PUBLICATIONS

NATL INST OF STANDARDS & TECH R.I.C.



A11102484894

Lewis, Richard L/An efficient and accurate method for calculating and representing power density in the near-zone of microwave antennas. U.S. GPO: 1985-3036-1. NBS-PUB-36

36

AN EFFICIENT AND ACCURATE METHOD FOR CALCULATING AND REPRESENTING POWER DENSITY IN THE NEAR-ZONE OF MICROWAVE ANTENNAS

Richard L. Lewis
Allen C. Newell

National Bureau of Standards
U.S. Department of Commerce
Boulder, Colorado 80303

December 1985

QC
100
.U56
85-3036
1986

Reg-NB
2/1/86
-USG
12/05/85
1082

NBSIR 85-3036

AN EFFICIENT AND ACCURATE METHOD FOR CALCULATING AND REPRESENTING POWER DENSITY IN THE NEAR-ZONE OF MICROWAVE ANTENNAS

Richard L. Lewis
Allen C. Newell

Electromagnetic Fields Division
Center for Electronics and Electrical Engineering
National Engineering Laboratory
National Bureau of Standards
Boulder, Colorado 80303

December 1985



U.S. DEPARTMENT OF COMMERCE, Malcolm Baldrige, Secretary

NATIONAL BUREAU OF STANDARDS, Ernest Ambler, Director

CONTENTS

	Page
I. Introduction.....	1
II. A Quick Method for Estimating Near-Zone Field Intensities Radiated by Circular Aperture Antennas.....	2
III. Computation of the Electric Field Intensity in the Near-Zone of Aperture Antennas by Numerical Integration of the Plane- Wave Spectrum.....	17
Appendix.....	25
References.....	27

An Efficient and Accurate Method for Calculating and Representing Power Density in the Near-Zone of Microwave Antennas

Richard L. Lewis & Allen C. Newell

An algorithm is presented for calculating near-zone and Fresnel-region fields in front of microwave antennas from discrete numerical values of the radiated plane-wave spectrum (complex far-field pattern). That is, the near fields are calculated by numerically integrating the plane-wave spectrum representation of the field. The crux of the analysis consists of handling a numerical instability which arises from integrating discrete data. A criterion is developed for limiting the integration domain in order to exclude highly oscillatory regions of the integrand. In turn, this leads to restricting the applicable output range over which the field can be computed. With the numerical instability problem thus resolved, fast Fourier transform techniques are used to assure efficient numerical integration over a large (but restricted) output range. The results are conveniently presented as relative power-density contours in planes formed by the longitudinal coordinate axis and one transverse coordinate axis. The algorithm is capable of extremely high accuracy, which is demonstrated by comparing predicted and measured near fields for two distinct antennas, along with a comparison against an exact theoretical model. In the case of circularly symmetric excitation models for electrically large antenna apertures, the predicted relative near-zone power-density contour plots turn out to be a function of just the relative aperture distribution. Nomographs for obtaining absolute near-zone power densities are presented for a few typical aperture-distribution functions.

Key words: antennas; antenna apertures; near fields; Fresnel region; plane-wave spectrum.

I. Introduction

There are a number of situations related to safety and interference where it is desirable to have a reliable and concise method of estimating the power density levels radiated by microwave antennas. We present a new technique for predicting near-zone field intensities using plane wave scattering matrix theory to produce accurate calculations along with a highly efficient method of graphically representing the results. Using this technique, comparisons of predicted and measured near fields were carried out for selected antennas and found to be in excellent agreement.

The input to the calculations is the far-field pattern (plane-wave spectrum) of the antenna obtained from either measured near-field data, design specifications, or theoretical analysis. From this input, programs based on the plane-wave theory were developed to calculate the field along the x and y axes on a series of planes parallel to the aperture. Then the power-density values in the x - z and y - z planes are obtained and graphically represented on two contour plots. The ordinate of these graphs covers the range $\pm 4D$ in units of D and the abscissa extends from just in front of the antenna out to D^2/λ in units of D^2/λ , where D is the antenna diameter and λ is the wavelength. This

choice of scaling means that a single graph will apply without approximation to all antennas with the same D/λ ratio and relative aperture distribution. Different input power levels can be accounted for by scaling.

Theoretical results are presented in section II of this report ignoring small structure effects (which frequently do not scale with D/λ), producing graphical presentations which just depend on the relative aperture distribution regardless of the D/λ ratio. The computational method is presented in section III, which concludes with specific examples using measured data to demonstrate the accuracy of this technique.

II. A Quick Method for Estimating Near-Zone Field Intensities Radiated by Circular Aperture Antennas

There are many instances where an estimate is needed of the near-zone field intensity radiated by a parabolic dish. One possible need is to evaluate hazards to personnel, explosive detonators, or sensitive electronics. A goal of the U.S. Environmental Protection Agency (EPA) is to characterize field intensity levels in the near field of typical aperture or reflector antennas. On behalf of the EPA, the U.S. National Bureau of Standards (NBS) has developed techniques for predicting antenna near fields. A few of these predictions are compared against near-field measurements for specific antennas and found to be in excellent agreement. Here, we wish to characterize near-zone field intensity levels for a specific class of antennas using these techniques.

Our near-field-prediction procedure is numerical integration of the plane-wave-spectrum integral representation for the electric field. The plane-wave spectrum data used by this procedure can be generated either from measured data or analytical models. In this study, we consider relative aperture distribution functions which are amenable to analytical integration to obtain theoretical plane-wave spectra.

We have chosen for study a circular aperture with a rotationally symmetric tapered aperture illumination. We wish to plot relative near-zone power densities as a function of (normalized) y and z coordinates, where z is measured along an axis perpendicular to the antenna aperture while y is measured in a plane transverse to the z axis. The expected antenna pattern is a function of $\frac{D}{\lambda} \sin\theta$, where D is the antenna diameter, λ is the wavelength, and θ is the angular position of the observation point with respect to antenna boresight.

Consequently, upon normalizing boresight distance z with respect to D^2/λ and transverse distance y with respect to D , we find that a single set of curves becomes sufficient to describe the relative near-field antenna pattern for a given D/λ ratio and a given relative aperture distribution. Moreover, if the maximum transverse distance y_{\max} is small compared to $\frac{D^2}{\lambda}$ (we assume $D \gtrsim 30\lambda$ and $y_{\max} \cong 4D$), then the near-field patterns become invariant with respect to D/λ . When $D < 30\lambda$ a separate near-field pattern for each D/λ value is required. Fortunately, the patterns change slowly so one can interpolate between just a few patterns.

One relative aperture distribution considered is $[1 - (\rho/a)^2]^2$, where ρ is the radial-distance variable in the aperture, $0 \leq \rho \leq a$, and $a = D/2$. Figure 1 shows this distribution's relative power-density contours in the y - z plane for the case $D \gtrsim 30\lambda$, where $-4D \leq y \leq 4D$ and $0 \leq z \leq D^2/\lambda$. Each contour corresponds to increments of 2.5 dB below the peak field intensity; the darker contours correspond to increments of 5 dB below the peak field intensity.

With a rotationally symmetric aperture distribution the contours at positive and negative y values will be mirror images. Thus, we only need the range $0 \leq y \leq 4D$. Also, using this range doubles the accuracy of specifying the graph ordinate y . The result using the same case as figure 1 is shown in figure 2. Overlaying the contours in figure 2 are dashed lines corresponding to constant y values, with incremental spacing of $\frac{D}{3}$ between adjacent lines. In figure 3 the relative field intensity along each of these lines is plotted as a set of parametric curves. The uppermost curve in figure 3 corresponds to $y = 0$.

The preceding figures describe the case $D \gtrsim 30\lambda$. To indicate how the results change for smaller $\frac{D}{\lambda}$ ratios, in figures 4, 5, and 6 we show relative y - z plane power-density contours for $\frac{D}{\lambda}$ values equal to 24, 16, and 10, respectively. Relatively little difference exists between figures 2 and 4, whereas considerable difference exists between off-boresight contours in going from figure 2 to figure 6. For further comparison, in figures 7 and 8 we show relative field intensity curves, along equally-spaced parallel lines analogous to figure 3, for $\frac{D}{\lambda}$ values of 16 and 10, respectively.

The absolute power density in dBm per square centimeter at any point in front of the antenna, for one watt of input power at the antenna aperture, is readily arrived at by combining the relative dB reading obtained from the preceding figures with the quantity, $38.57 - 20 \times \text{Log}_{10} D$ [dBm/cm²], where D is in centimeters.

We next present results for a slightly modified relative aperture distribution, of the form $\alpha + [1 - (\frac{\rho}{a})^2]^2$, where α is a small constant. Thus, in figures 9 and 10 we present relative power density contours and relative field-intensity curves for $\alpha = 0.1$ (a pedestal 20 dB down), while in figures 11 and 12 we present results for $\alpha = 0.316$ (a pedestal 10 dB down). In the first case the absolute power density in dBm/cm² for one watt of input power at the antenna aperture is arrived at by combining the relative dB reading obtained from figure 9 or 10 with $38.17 - 20 \times \text{Log}_{10}D$, while for the second case the absolute power density is obtained by combining the relative dB reading from figure 11 or 12 with $38.14 - 20 \times \text{Log}_{10}D$. Again, D is in centimeters.

To illustrate the use of these graphs, assume that the antenna is a 11.3 m (37 ft) diameter parabolic reflector operating at 6.5 GHz with 56 kW of input power, and that we wish to estimate the power density 823 m (2700 ft) out from the antenna face and 15.2 m (50 ft) off axis. Thus, the y distance is $1.35D$ and the z distance is $0.3\frac{D^2}{\lambda}$. From figure 2, we see that at these coordinates there is a relative power density of -45 dB relative to the peak, an amount also confirmed by figure 3. The corresponding absolute power density per watt of input power is -67.5 dBm/cm², so the actual power density is about 0.01 mW/cm² at this location. The effect here of a pedestal in the relative aperture distribution is destructive interference according to figures 9 and 11, so the above estimate may be considered as worst case.

In conclusion then, we have presented a nomograph and associated algorithm for obtaining the absolute power density in the near field of a circular aperture with a $[1 - (\frac{\rho}{a})^2]^2$ relative aperture distribution, along with results for this distribution on a 10 dB pedestal and on a 20 dB pedestal. It should be noted, in extrapolating these results to actual antennas, that aperture blockage and struts will produce additional effects that have not been accounted for here.

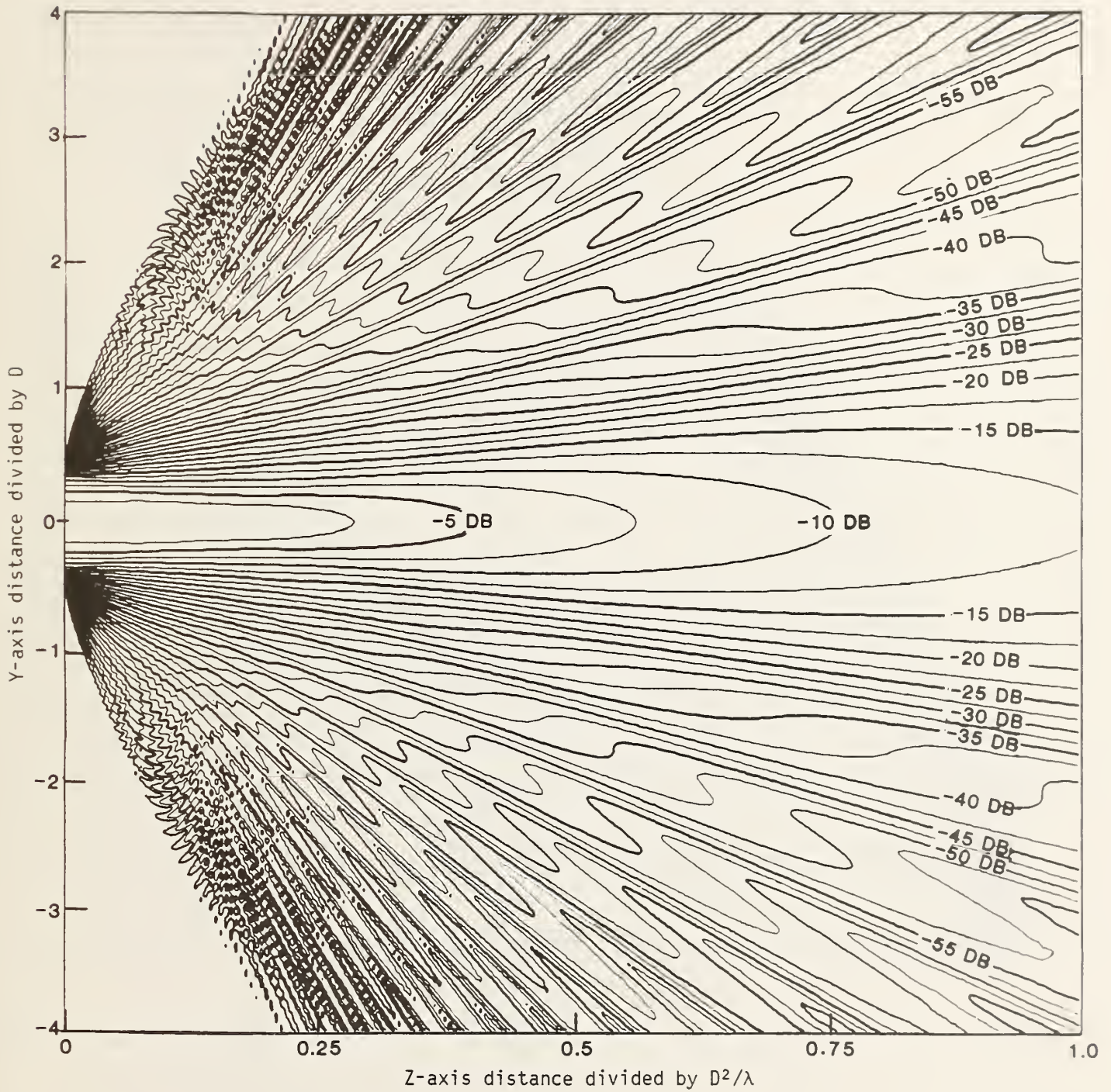


Figure 1. Relative Power Density Contours in the Y-Z plane for a $[1 - (\frac{\rho}{a})^2]^2$ aperture distribution: $D > 30\lambda$; $-4D$ to $+4D$ range on Y.

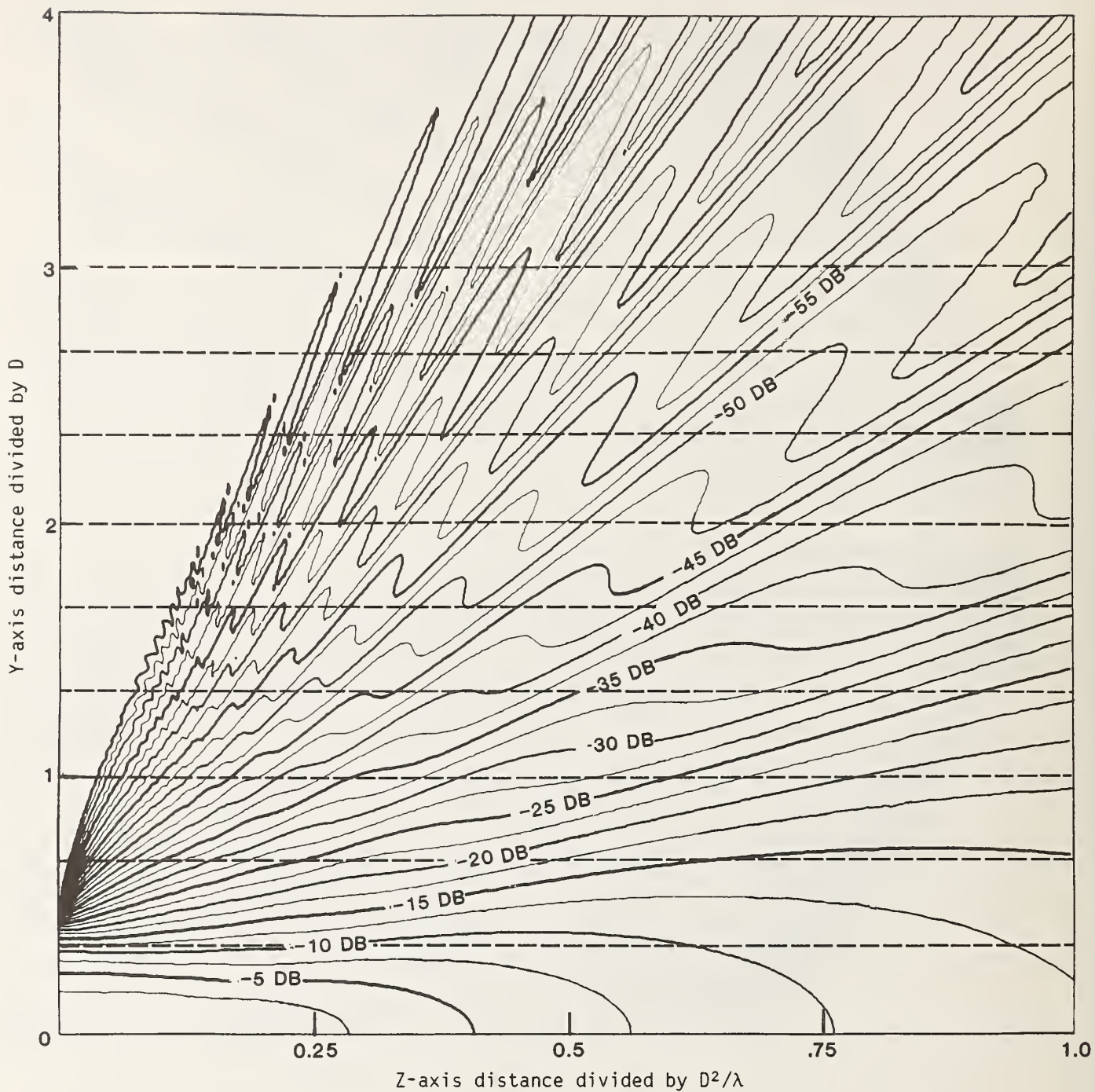


Figure 2. Relative Power Density Contours in the Y-Z plane for a $[1 - (\frac{D}{a})^2]^2$ aperture distribution: $D > 30\lambda$.

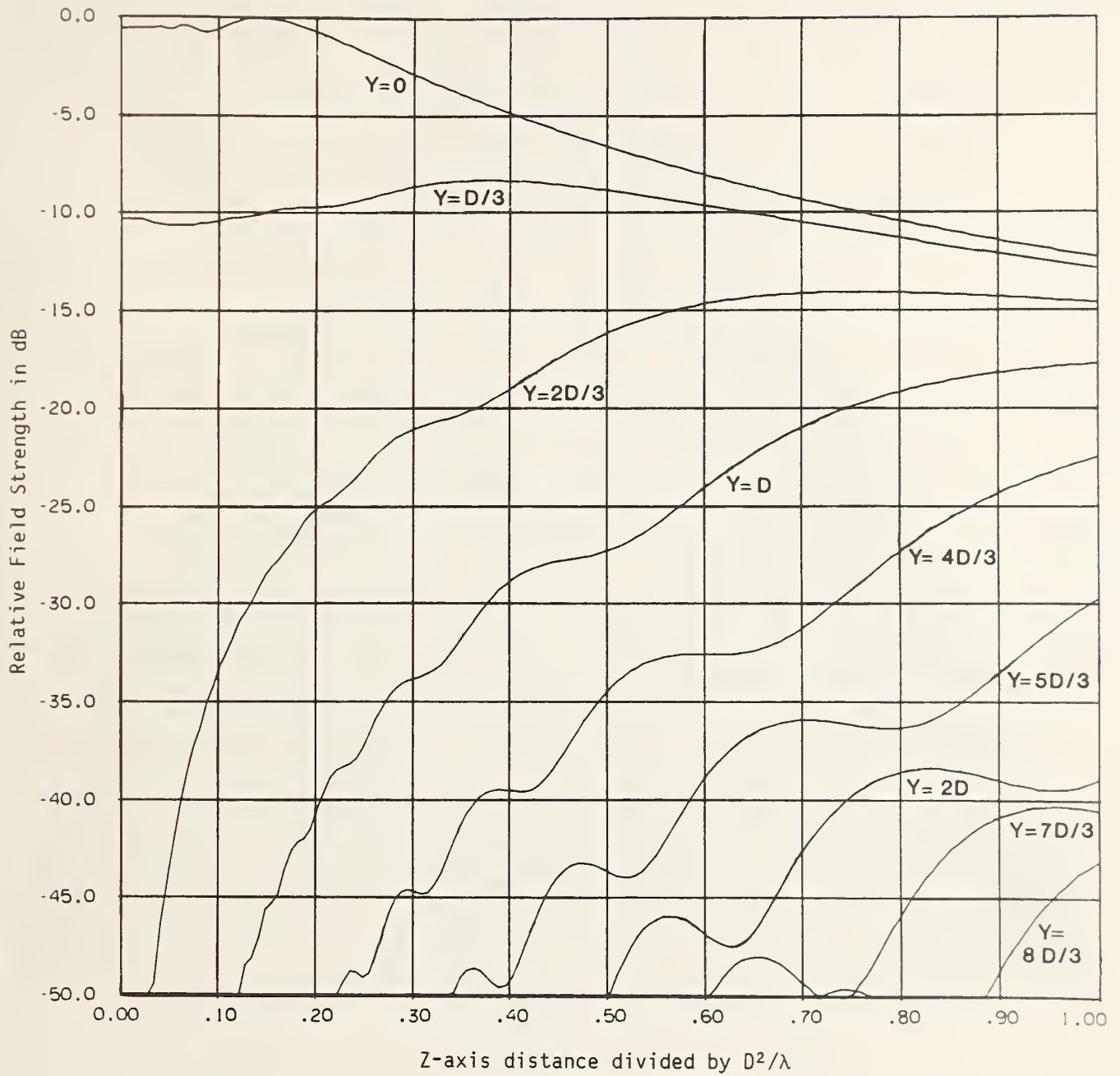


Figure 3. Relative Field Intensity along equally spaced parallel lines for a $[1 - (\frac{\rho}{a})^2]^2$ aperture distribution: $D > 30\lambda$.

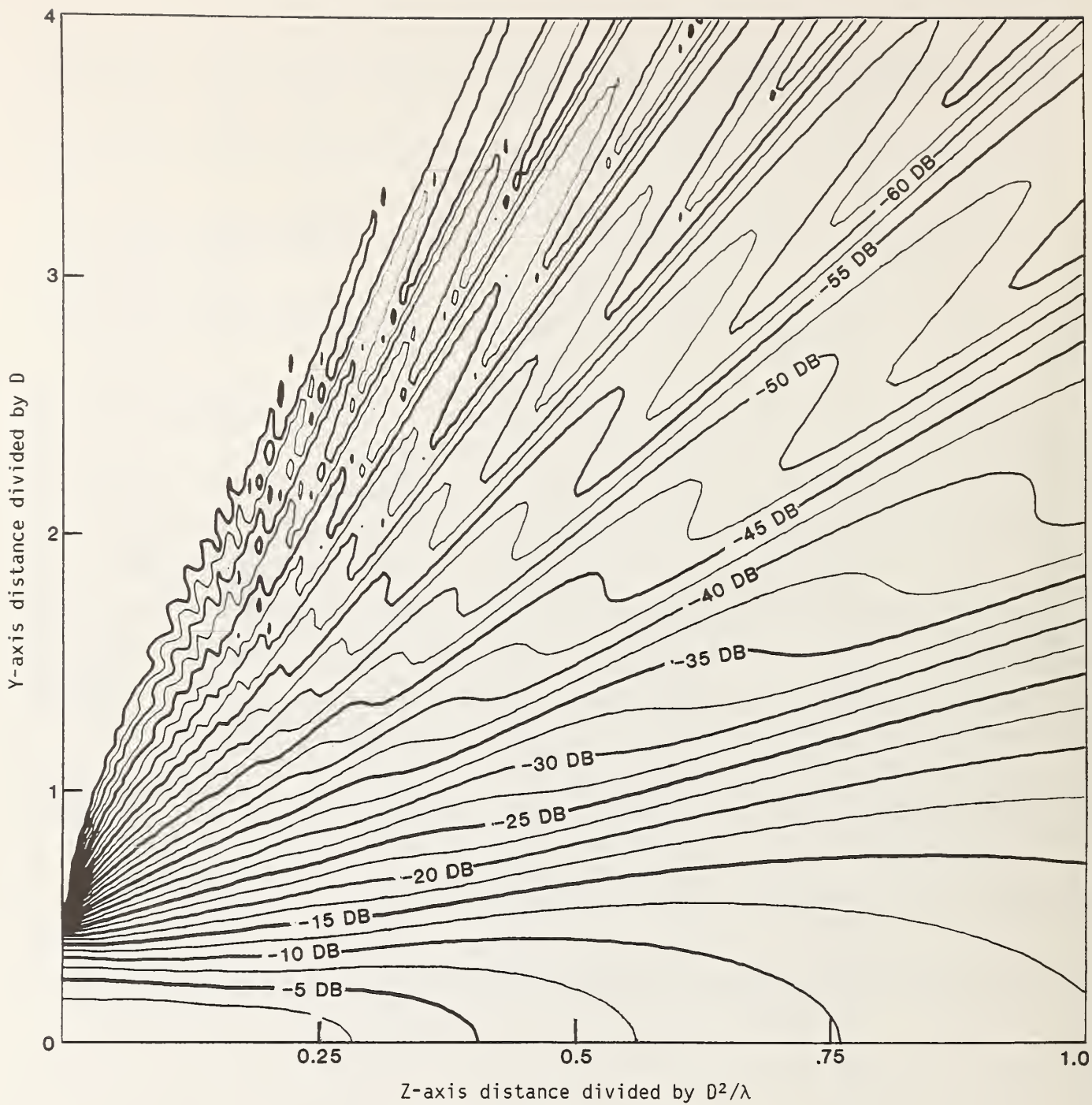


Figure 4. Relative Power Density Contours in the Y-Z plane for a $[1 - (\frac{\rho}{a})^2]^2$ aperture distribution: $D = 24\lambda$.

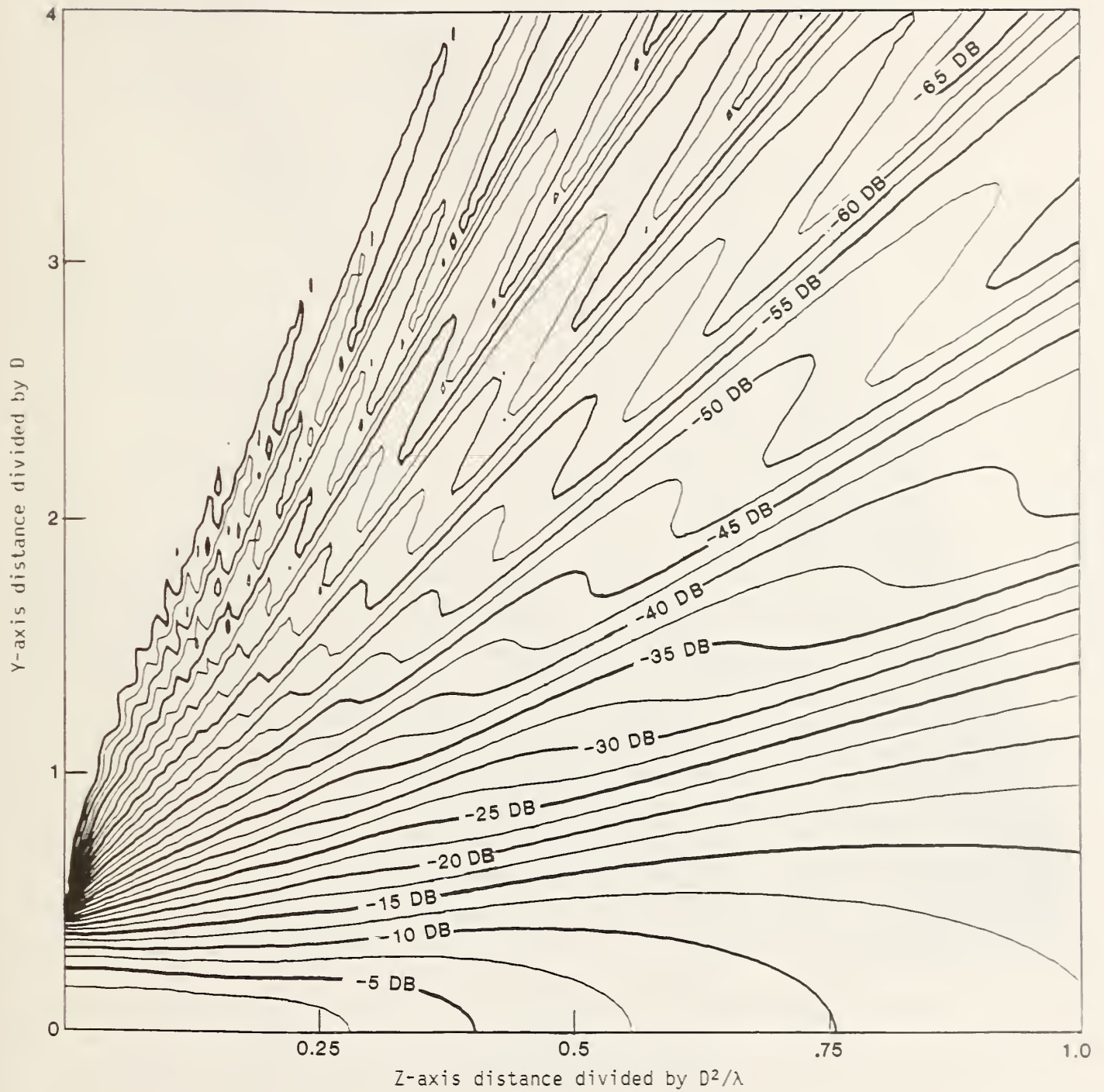


Figure 5. Relative Power Density Contours in the Y-Z plane for a $[1 - (\frac{D}{a})^2]^2$ aperture distribution: $D = 16\lambda$.

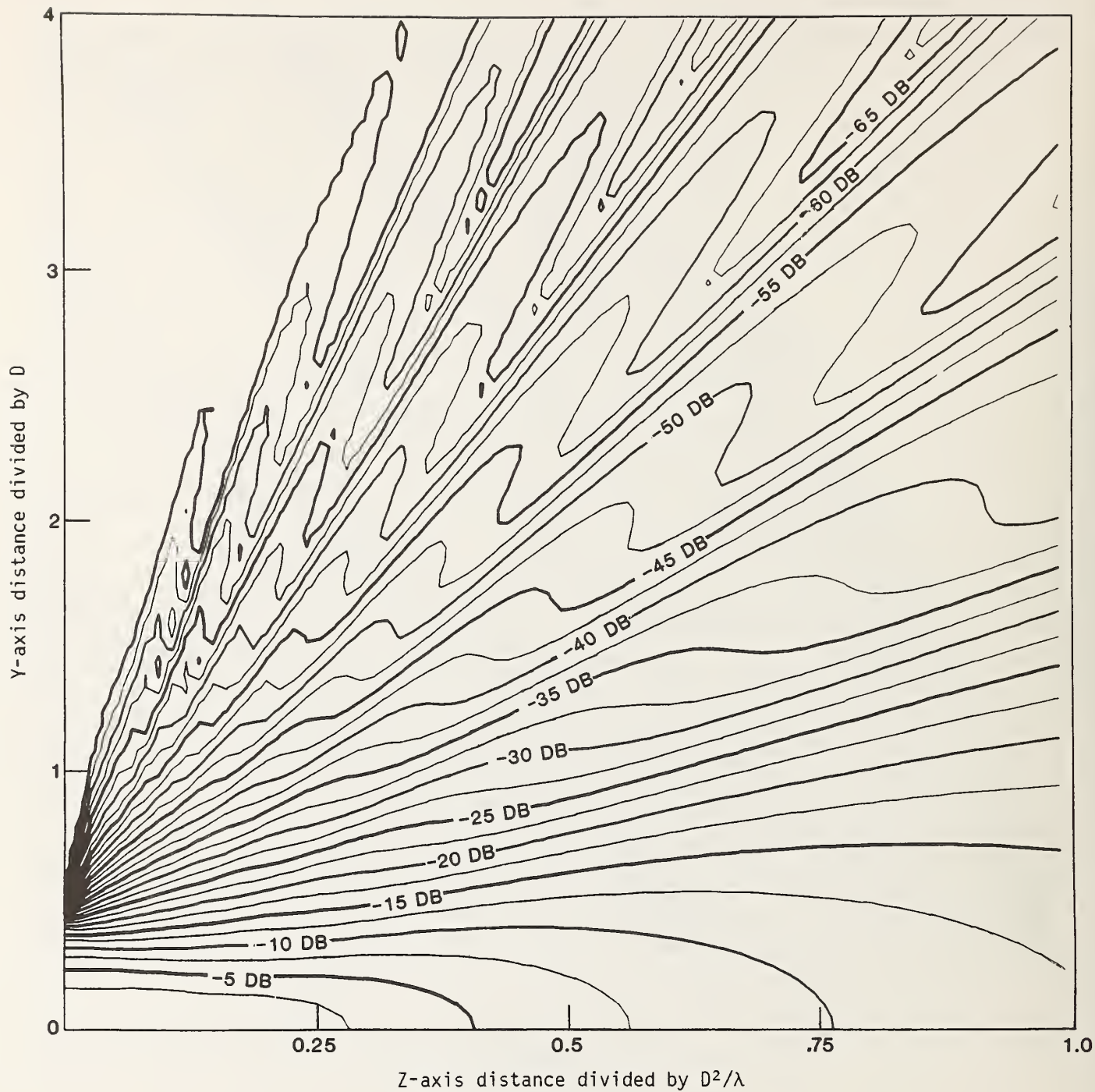


Figure 6. Relative Power Density Contours in the Y-Z plane for a $[1 - (\frac{\rho}{a})^2]^2$ aperture distribution: $D = 10\lambda$.

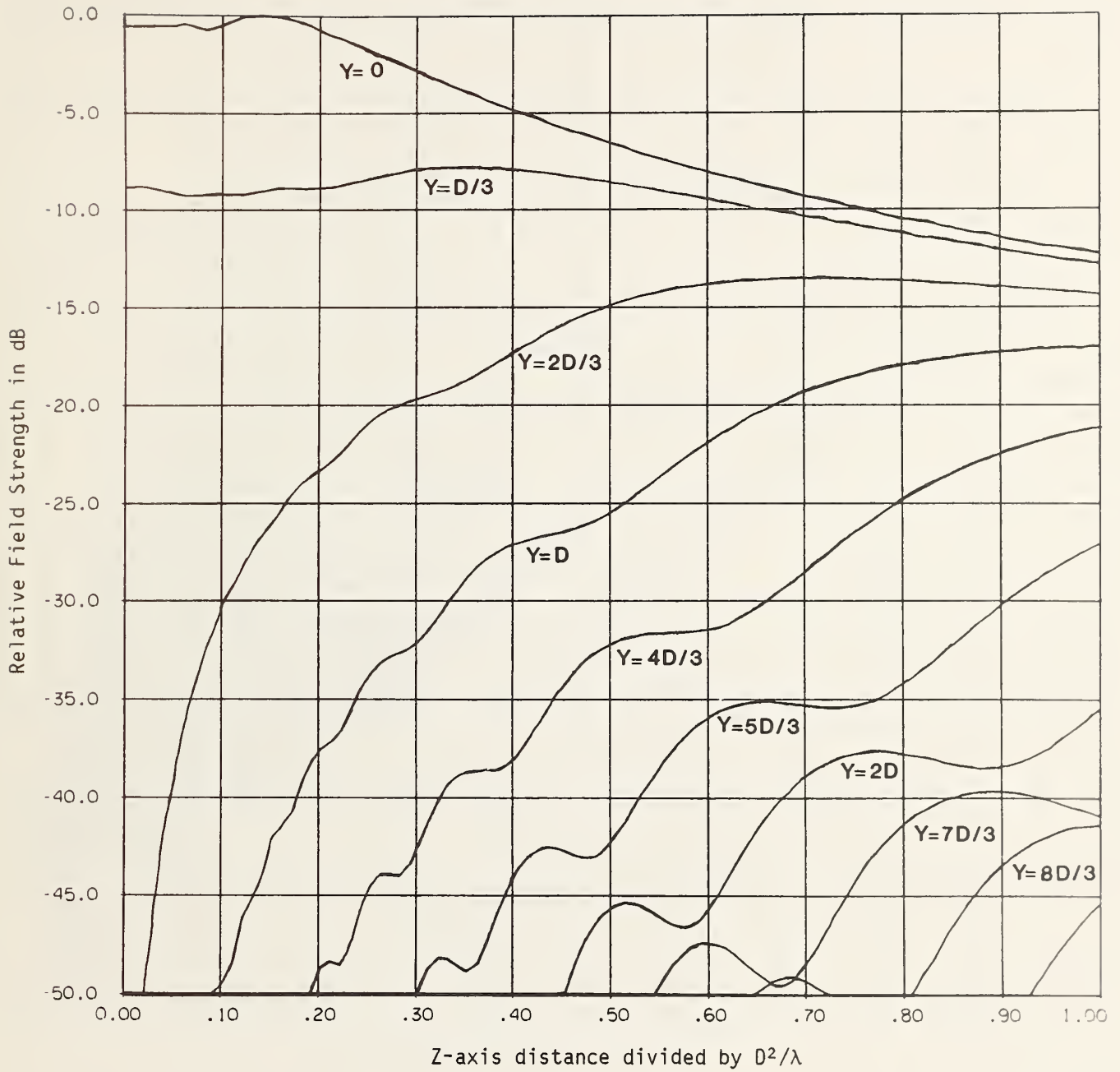


Figure 7. Relative Field Intensity along equally spaced parallel lines for a $[1 - (\frac{\rho}{a})^2]^2$ aperture distribution: $D = 16\lambda$.

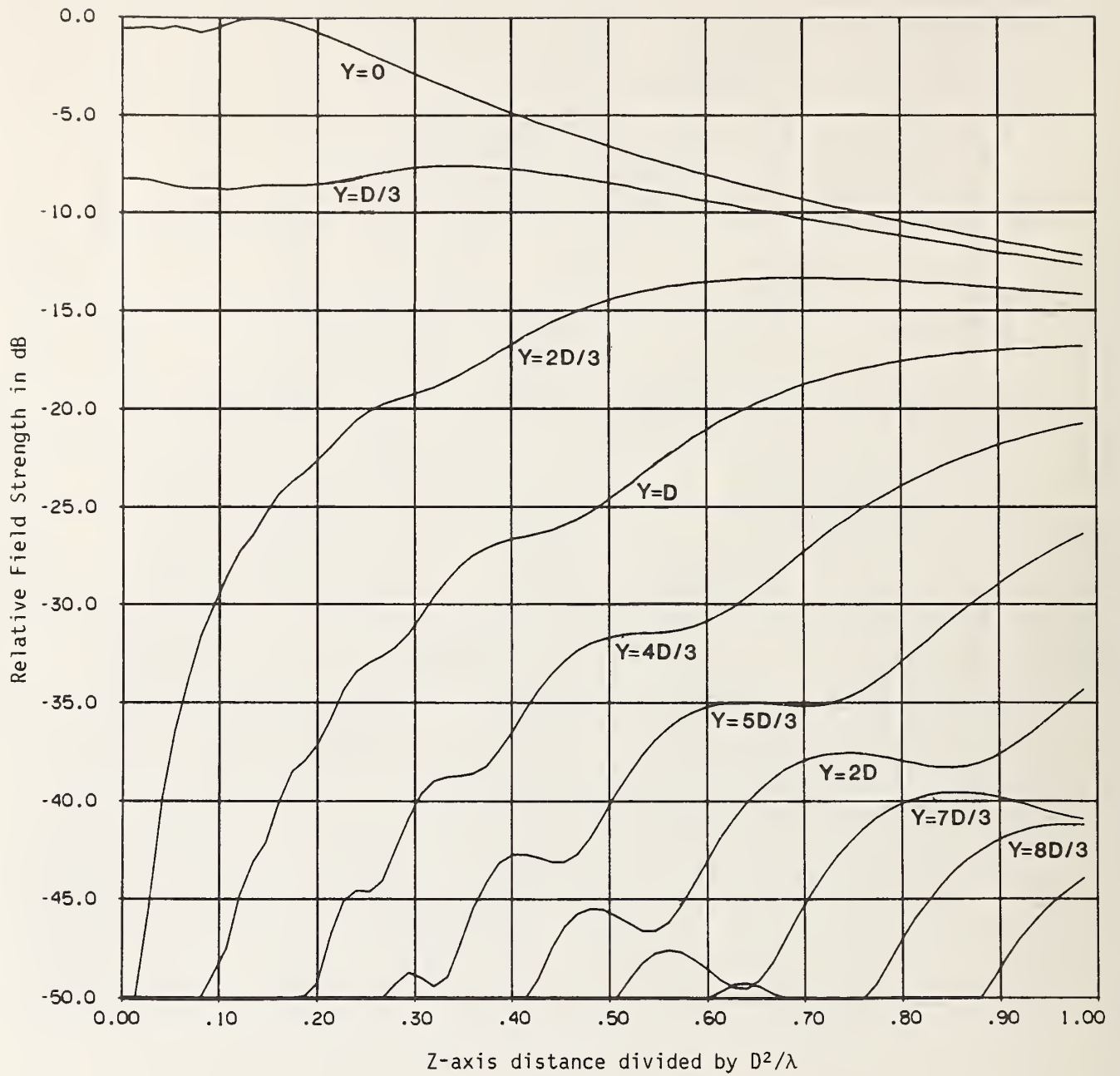


Figure 8. Relative Field Intensity along equally spaced parallel lines for a $[1 - (\frac{\rho}{a})^2]^2$ aperture distribution: $D = 10\lambda$.

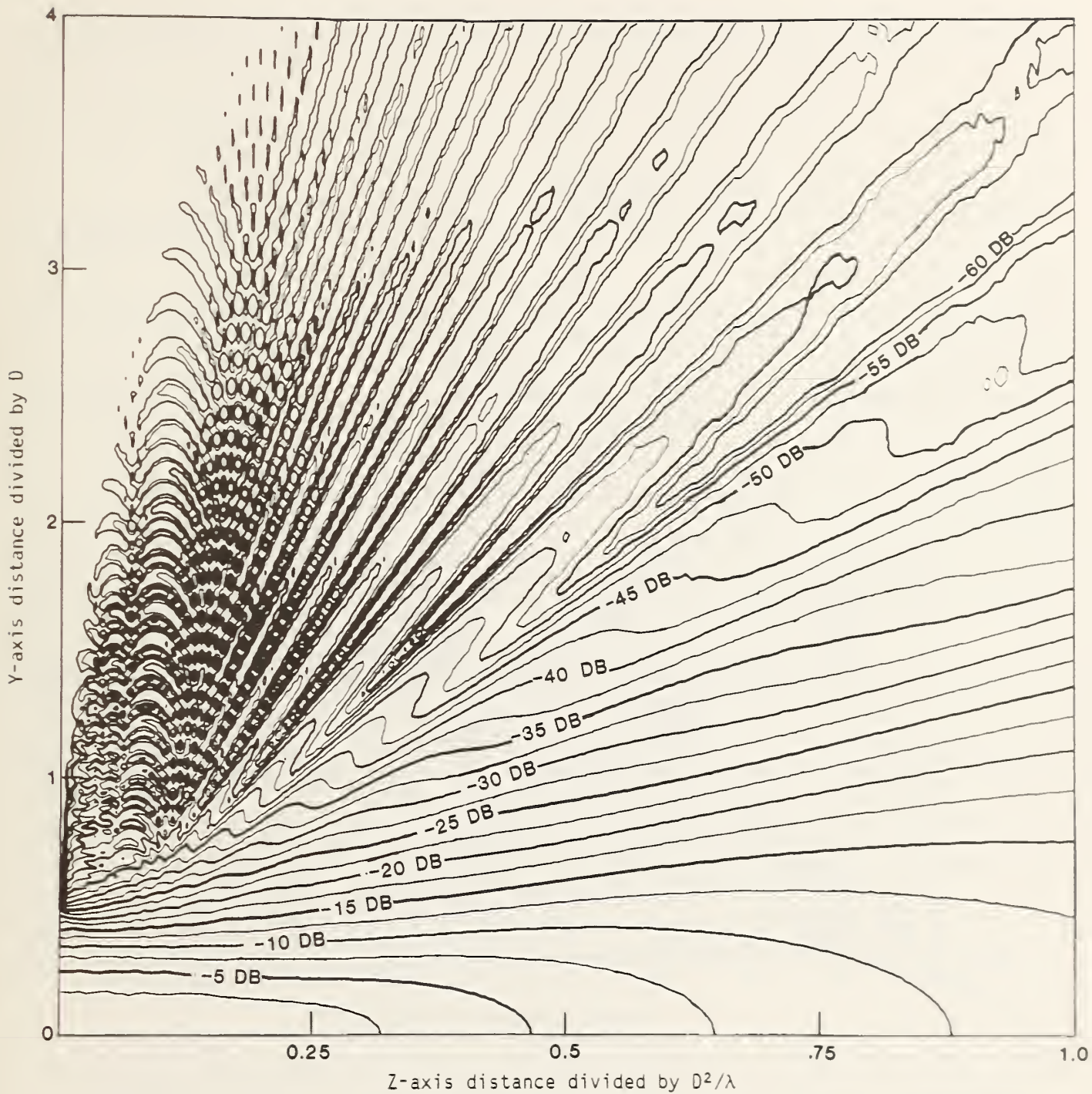


Figure 9. Relative Power Density Contours in the Y-Z plane for a $[1 - (\frac{r}{a})^2]^2$ aperture distribution on a pedestal 20 dB down: $D > 30\lambda$.

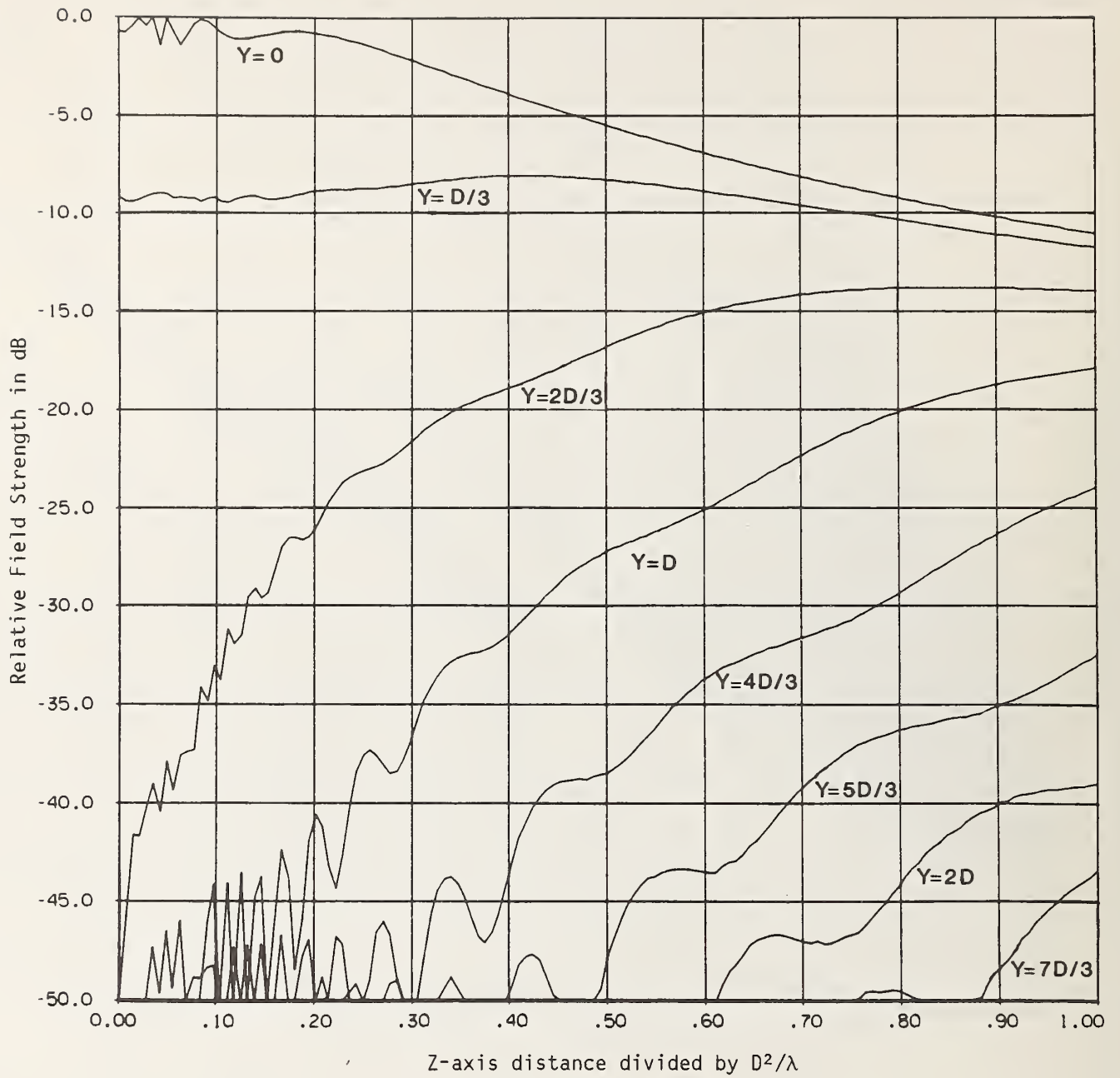


Figure 10. Relative Field Intensity along equally spaced parallel lines for a $[1 - (\frac{\rho}{a})^2]^2$ aperture distribution on a pedestal 20 dB down: $D > 30\lambda$.

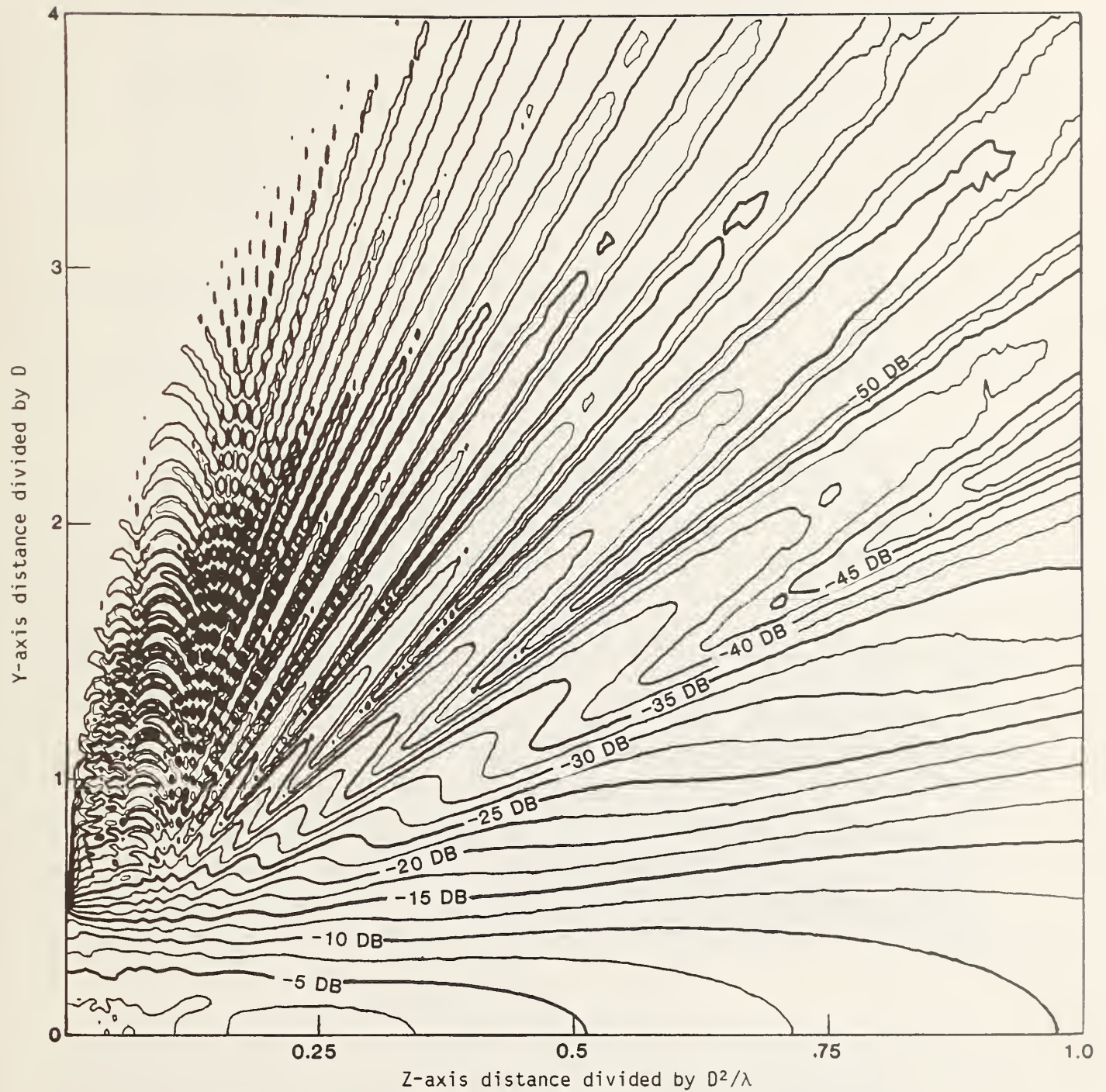


Figure 11. Relative Power Density Contours in the Y-Z plane for a $[1 - (\frac{\rho}{a})^2]^2$ aperture distribution on a pedestal 10 dB down: $D > 30\lambda$.

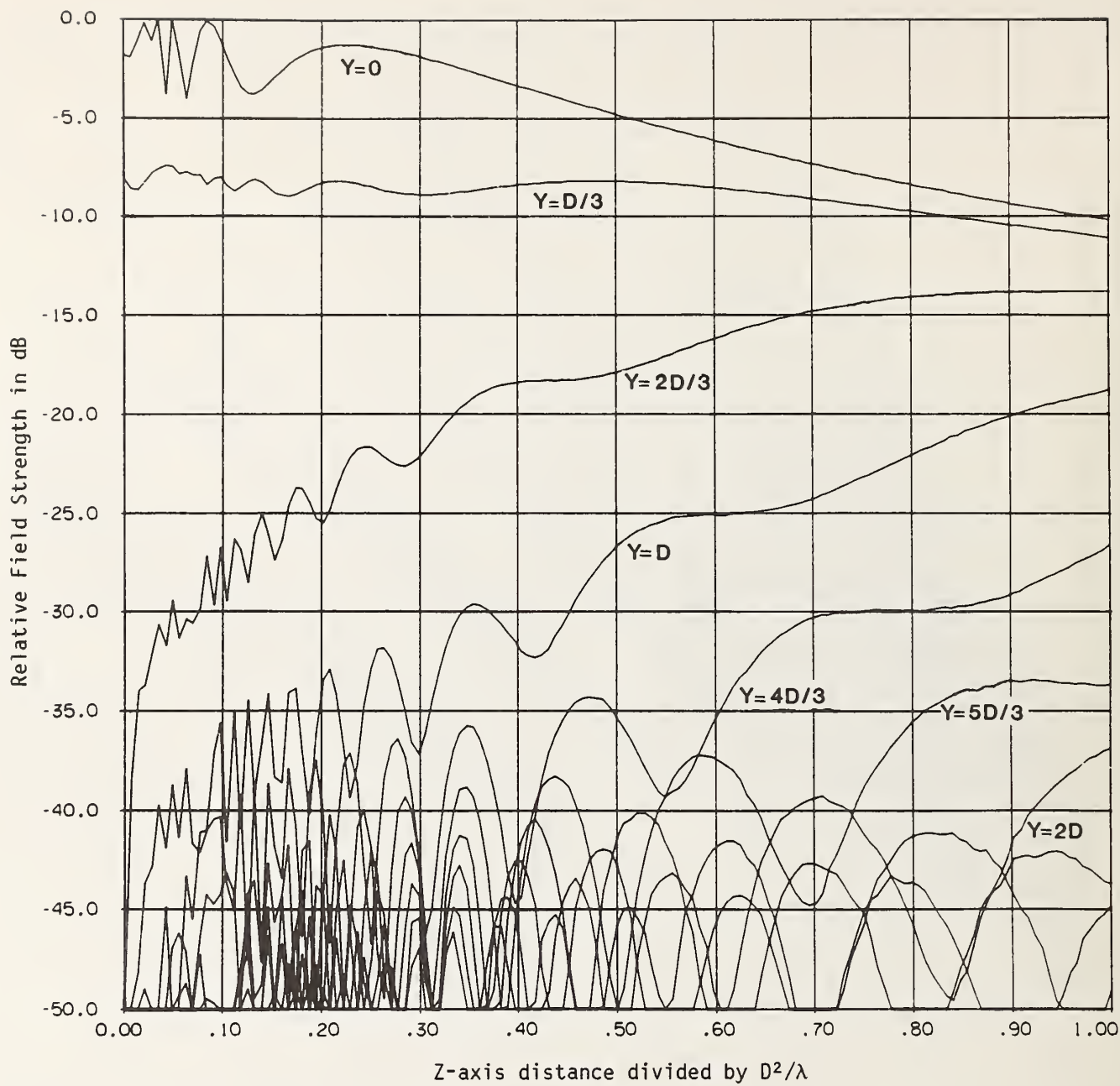


Figure 12. Relative Field Intensity along equally spaced parallel lines for a $[1 - (\frac{\rho}{a})^2]^2$ aperture distribution on a pedestal 10 dB down: $D > 30\lambda$.

III. Computation of the Electric Field Intensity in the Near-Zone of Aperture Antennas by Numerical Integration of the Plane-Wave Spectrum

Considerable attention has been given to the problem of calculating the far-field pattern of an antenna from measured near-field data [1] - [11]. Of these techniques, planar near-field scanning (plane-wave spectrum deconvolution) has seen the most development [12] - [16]. Here, we wish to consider the inverse problem of determining near-zone and Fresnel region fields from numerical values of the complex, vector, far-field pattern. That is, we are interested in numerical evaluation of the plane-wave spectrum integral representing the radiated electric field. We assume that numerical plane-wave spectrum data has previously been generated either from planar near-field measurements or from theoretical far-field patterns.

An earlier algorithm was developed by Yaghjian [17] for carrying out such a numerical integration. In Yaghjian's analysis, the integration domain was restricted in order to achieve computational efficiency; this also served to constrain the oscillatory nature of the integrand and so eliminate a catastrophic numerical instability which otherwise occurs at large z-axis distances with discrete data points. Use of the fast Fourier transform (FFT) provides efficient numerical integration over a large transverse output range.

Extending this earlier work to measured data with fixed data-point spacing and to z-axis distances greater than $0.5 \frac{D^2}{\lambda}$, where D is the antenna diameter and λ is the wavelength, we found that numerical instabilities appeared at the extremities of the integration range. Attempts to reduce these instabilities by uniformly decreasing the already restricted integration domain drove the calculated field to zero at the extremities, an effect that had also been found by Yaghjian [17]. In order to compensate for these computational difficulties, a new limiting criterion was developed.

In Yaghjian's analysis, a geometrical (sheaf of angles) criterion was used to limit the integration domain. In this work, we develop an improved formula for limiting the integration domain, using a sampling-theorem [18] criterion, producing a numerically more-stable result over a greater cartesian-coordinate output range. Also, we establish upper bounds on the z-axis distance from the antenna and on the data-point spacing interval (Δ) of the plane-wave spectrum in order to ensure reliable computations.

Evaluating the plane-wave spectrum integral, then, we compute near-zone and Fresnel-region fields at a sequence of fixed z-axis distances as a

function of the lateral coordinates x and y . We reduce computational effort by alternately setting one lateral coordinate equal to zero. By computing along just the x and y axes we obtain sufficient data to generate near-zone field-intensity contours in the x - z and y - z planes. The maximum lateral coordinate range is $R_0 = \frac{\pi}{\Delta}$. However, we empirically determined that an effective lateral coordinate range about half this size is needed to avoid numerical instabilities. Thus, this effective lateral coordinate range and the upper bound on the z -axis distance together define a truncated cylindrical region bounding the near-field computation domain.

Yaghjian [17] describes how a coordinate-system rotation of the plane-wave spectrum data allows the cylindrical region's axis to subtend an arbitrary angle with respect to the main beam of the antenna; however, this also results in having to interpolate when using discrete plane-wave spectrum data. Here, by aligning the cylindrical region's axis with the perpendicular to the near-field measurement plane, interpolation becomes unnecessary and so we avoid interpolation error.

To be definite, we describe the case where the plane-wave spectrum data are obtained from planar near-field measurements. The antenna measurement setup is depicted in figure 13, showing the antenna under test, the near-field measurement plane with the probe antenna just in front of the test antenna, and a hypothetical y - z plane cut through the cylindrical region of interest. Graphical output is represented in the figure by field-strength contours in the y - z plane. At equally spaced intervals along the z -axis, vertical dashed lines are drawn to represent the series of y -axis cuts along which the near field is computed by the planar near-field program. For smooth contours, of course, many more plane-cut computation points would be required along the z -axis than are indicated by the figure.

As background, and to introduce notation, we give an expression for the y -component of a transmitting antenna's plane-wave spectrum in terms of measured probe data taken over a planar surface in front of the antenna. It is assumed that multiple reflections between the transmitting antenna and the probe are negligible, that both antennas are polarization matched in the same (y) direction, that the input reflection coefficients at the waveguide leads to the antennas are negligible, and that the probe is far enough removed from the transmitting antenna so that the significant probe receiving pattern is independent of spatial frequency variations, i.e., the incident radiation at the probe has a relatively narrow angle of arrival. Let $B_0(\underline{P})$ be the signal received by the probe at position \underline{P} on the planar scan surface normalized to

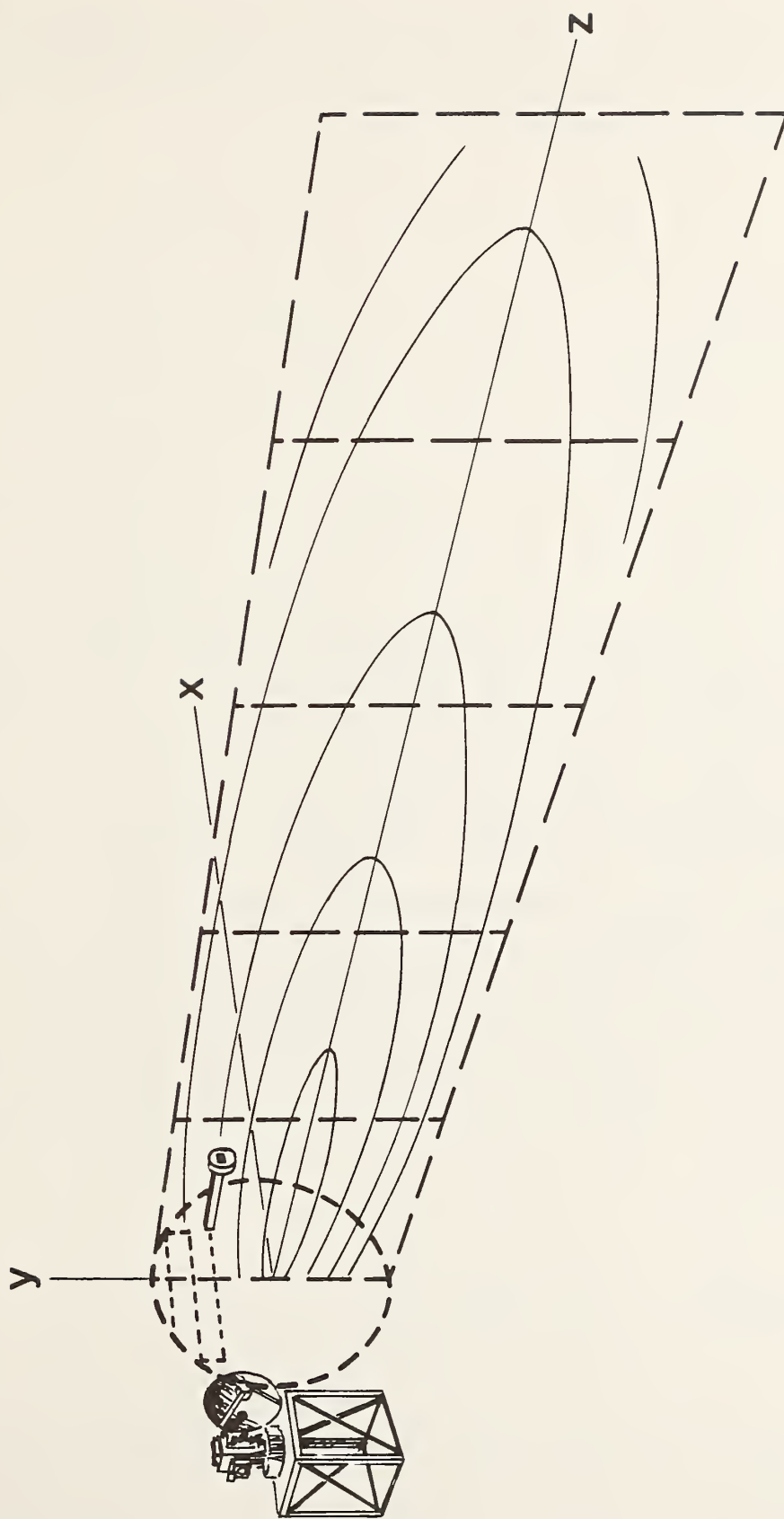


Figure 13. Antenna Measurement Setup Showing Near-Zone Y-Z Plane Cut on which the Field-intensity Contours are Plotted.

unity at position \underline{P}' (here, $\underline{P} = x\underline{a}_x + y\underline{a}_y$, where \underline{a}_x , \underline{a}_y , \underline{a}_z are unit cartesian vectors), and let A_0 be the insertion loss between the transmitting antenna and the probe when it is located at position \underline{P}' . Then the plane-wave spectrum's y-component can be expressed [12,13] as

$$b(\underline{K}) = \frac{1}{\lambda} \sqrt{\frac{2P_0}{\pi A_0 Y_0 G_r(o)}} e^{-i\gamma d} \iint_{-\infty}^{\infty} B_0(\underline{P}) e^{-i\underline{K} \cdot \underline{P}} d\underline{P}, \quad (1)$$

where P_0 is the input power to the antenna, Y_0 is the characteristic admittance of free space, $G_r(o)$ is the gain of the probe, d is the z-axis distance from the planar scan surface to the transmitting antenna, $d\underline{P} = dx dy$, λ is the wavelength, $\underline{K} = k_x \underline{a}_x + k_y \underline{a}_y$, and $\gamma = \sqrt{k^2 - K^2}$ where $k = 2\pi/\lambda$ and $K^2 = \underline{K} \cdot \underline{K}$.

The function $B_0(\underline{P})$ is virtually representable (i.e., $b(\underline{K})$ approaches zero for K sufficiently greater than k , depending upon d) as the Fourier transform of a bandlimited function. Consequently, the sampling theorem applies, so the double integral (1) is completely determined by the sampling of data at discrete equal-spaced lattice points over the scan plane [12]. If we assign band limits $\pm k_{xm}$ and $\pm k_{ym}$ to k_x and k_y , respectively, then (1) becomes [ibid]

$$b(\underline{K}) = \frac{1}{\lambda} \sqrt{\frac{2P_0}{\pi A_0 Y_0 G_r(o)}} e^{-i\gamma d} \frac{\pi^2}{k_{xm} k_{ym}} \sum_{r=-N_1}^{N_1} \sum_{s=-N_2}^{N_2} B_0(\underline{P}_{rs}) e^{-i\underline{K} \cdot \underline{P}_{rs}},$$

where $\underline{P}_{rs} = \frac{r\pi}{k_{xm}} \underline{a}_x + \frac{s\pi}{k_{ym}} \underline{a}_y$. To be mathematically exact, N_1 and N_2 should be infinite; in practice, N_1 and N_2 are limited by the size of the scan area. As given above, the FFT would limit to $2N_1 \times 2N_2$ the number of points at which values of $b(\underline{K})$ would be calculated. However, we increase the output spectral density (number of data points) by zero filling around the scan area boundary. Thus, setting $B_0(\underline{P}_{rs}) = 0$ for $|r| > N_1$ or for $|s| > N_2$, we have

$$b(\underline{K}_{mn}) = \frac{1}{\lambda} \sqrt{\frac{2P_0}{\pi A_0 Y_0 G_r(o)}} e^{-i\gamma_{mn} d} \frac{\pi^2}{k_{xm} k_{ym}} \sum_{r=-\frac{N_x}{2}}^{\frac{N_x}{2}-1} \sum_{s=-\frac{N_y}{2}}^{\frac{N_y}{2}-1} B_0(\underline{P}_{rs}) e^{-i\underline{K}_{mn} \cdot \underline{P}_{rs}}, \quad (2)$$

where $-\frac{N_x}{2} \leq m \leq \frac{N_x}{2} - 1$, $-\frac{N_y}{2} \leq n \leq \frac{N_y}{2} - 1$. Here, $\underline{K}_{mn} = m\Delta_x \underline{a}_x + n\Delta_y \underline{a}_y$ and

$$\gamma_{mn} = \sqrt{k^2 - K_{mn}^2}, \text{ where } \Delta_x = \frac{2k_{xm}}{N_x}, \Delta_y = \frac{2k_{ym}}{N_y} \text{ and } N_x > 2N_1, N_y > 2N_2.$$

We now return to the development of the near-field computation algorithm. The electric field can be obtained at any point $\underline{r} = \underline{R} + z\underline{a}_z$, where $\underline{R} = x\underline{a}_x + y\underline{a}_y$, from the plane-wave spectrum integration

$$\underline{E}(\underline{r}) = \frac{1}{2\pi} \int \int_{-\infty}^{\infty} \underline{b}(\underline{K}) e^{i\underline{k} \cdot \underline{r}} d\underline{K} \quad (3)$$

where $\underline{k} = \underline{K} + \gamma\underline{a}_z$ and $d\underline{K} = dk_x dk_y$. Here we assume that the vector spectral-density function $\underline{b}(\underline{K})$ is known. If both the x and y components of $\underline{b}(\underline{K})$ have been determined, then the z component is obtained from $b_z(\underline{K}) = -\frac{1}{\gamma} \underline{K} \cdot \underline{b}(\underline{K})$. In the far-field of the antenna (3) becomes

$$\underline{E}(\underline{r}) \cong -ik \cos\theta \underline{b}\left(\frac{k}{r} \underline{R}\right) \frac{e^{ikr}}{r},$$

where $\cos\theta = z/r$ and $r = \sqrt{\underline{r} \cdot \underline{r}}$.

In the Fresnel region evanescent modes will not be significant, so the integration limits in (3) change from $\pm\infty$ to $\pm k$. The minimum applicable z distance is at least a few wavelengths to ensure that evanescent modes have attenuated. In our technique, the integration is carried out using the FFT for a single fixed value of z at a time. However, stability problems can become critical in carrying out a numerical integration. In particular, when z is moderately large, the factor $e^{i\gamma z}$ in the integrand can oscillate rapidly between plus and minus one while the rest of the integrand changes very little. As a result, these terms cancel out analytically, but with discrete data on a computer they can add numerically to produce a significant integration error. This can occur when z/D is as small as 2 or 3, where D is the antenna diameter. One can compensate for this by limiting the domain of integration even further, say to $-k_{x0} \leq k_x \leq k_{x0}$, $-k_{y0} \leq k_y \leq k_{y0}$, where $k_{x0} < k$, $k_{y0} < k$. That is, we have to evaluate the near-field expression

$$\underline{E}(\underline{r}) = \frac{1}{2\pi} \int_{-k_{x0}}^{k_{x0}} e^{ik_x x} dk_x \int_{-k_{y0}}^{k_{y0}} e^{i\gamma z} \underline{b}(\underline{K}) e^{ik_y y} dk_y \quad (4)$$

We obtain integration-domain limits for (4) by using sampling theorem criteria; namely, the maximum change in yz between two adjacent sample points shall be less than π . After some ado, this leads to the result

$$\frac{k_{x_0} + k_{y_0}}{k} \cong \frac{R_0}{\sqrt{R_0^2/\beta + z^2}} \quad (5)$$

where $R_0 \equiv \pi/\Delta_y \cong \pi/\Delta_x$. Here, $\beta = 1 + \sin 2\phi_0$ where $\phi_0 = \tan^{-1} k_{y_0}/k_{x_0}$. The derivation of (5) is presented in the appendix, where we establish that the maximum z distance is limited by $z < \frac{R_0^2}{\lambda}$.

Using the FFT to evaluate (4), it is expedient to integrate over the extended domain $|k_x| \leq k_{xm}$, $|k_y| \leq k_{ym}$, where $k_{xm} \cong k_{ym} \geq k$, and utilize a window function to limit the effective integration domain to $k_{x_0} < k_{xm}$, $k_{y_0} < k_{ym}$. Thus, for a fixed value of z , we can approximate (4) by

$$\underline{E}_{j,\ell} = \frac{\Delta_x \Delta_y}{2\pi} \sum_{m=-\frac{N_x}{2}}^{\frac{N_x}{2}-1} \sum_{n=-\frac{N_y}{2}}^{\frac{N_y}{2}-1} \underline{F}(m\Delta_x, n\Delta_y) \exp\{i2\pi(\frac{jm}{N_x} + \frac{\ell n}{N_y})\}. \quad (6)$$

Here, $\underline{E}_{j,\ell}$ is the Fresnel-region electric field in the x - y plane corresponding to a fixed value of z with $x = j\delta_x$, $y = \ell\delta_y$, where $\delta_x = \pi/k_{xm}$ and $\delta_y = \pi/k_{ym}$ correspond to measurement-plane data-point spacing increments. Also, $\underline{F}(k_x, k_y) = \underline{b}(\underline{K})u(\underline{K})e^{i\gamma z}$, where $u(\underline{K})$ is a window function for limiting the oscillatory behavior of $e^{i\gamma z}$. The extended integration domain limits are given by $k_{xm} = 1/2 N_x \Delta_x$, $k_{ym} = 1/2 N_y \Delta_y$. In (6), $-N_x/2 \leq j < N_x/2$, $-N_y/2 \leq \ell < N_y/2$, so the maximum lateral coordinate range is $|x| \leq 1/2 N_x \delta_x = \pi/\Delta_x$, $|y| \leq 1/2 N_y \delta_y = \pi/\Delta_y$. However, good numerical stability of (6) at moderately large z values limits the effective lateral coordinate range to about $|x| < 1/4 N_x \delta_x$, $|y| < 1/4 N_y \delta_y$.

Equation (5) was compared against an alternate expression obtained by Yaghjian [17]. Although (5) yielded the best results, it lacked the latter's ease of implementation. However, with a hybrid formula, we obtained an expression that yielded good results along with ease of computation. Accordingly, the window function $u(\underline{K})$ is set equal to zero under the condition

$$\frac{|k_x| + |k_y|}{k} > \frac{R_0 + D}{\sqrt{R_0^2 + z^2}}.$$

The integration cutoff imposed by $u(\underline{K})$ can lead to ringing at the extremities of the computed near field when the amplitude of $\underline{b}(\underline{K})$ at the cutoff point is large. This, in fact, is the reason for limiting the effective range on x and y to about half the normal FFT output range. Note that this range limitation quadruples the number of data points needed for the plane-wave-spectrum integration.

We now write (6) in a form more suitable for FFT processing. The result is

$$\underline{E}_{j - \frac{N_x}{2}, \ell - \frac{N_y}{2}} = \frac{\Delta_x \Delta_y}{2\pi} e^{-i(j+\ell)\pi} \sum_{m=0}^{N_x-1} \sum_{n=0}^{N_y-1} \{ \underline{F}[(m - \frac{N_x}{2})\Delta_x, (n - \frac{N_y}{2})\Delta_y] e^{i(m+n)\pi} \} \exp \{ i2\pi(\frac{jm}{N_x} + \frac{\ell n}{N_y}) \},$$

where the ranges $0 \leq j \leq N_x - 1$, $0 \leq \ell \leq N_y - 1$ apply. As a result, our formulation agrees with standard FFT practice. It is assumed that $N_x/2$ and $N_y/2$ are both even integers.

In case we are interested in the field along the y -axis where $x = 0$, the preceding expression becomes

$$\underline{E}_{0, \ell - \frac{N_y}{2}} = \frac{\Delta_x \Delta_y}{2\pi} e^{-i\ell\pi} \sum_{n=0}^{N_y-1} e^{in\pi} \left\{ \sum_{m=0}^{N_x-1} \underline{F}[(m - \frac{N_x}{2})\Delta_x, (n - \frac{N_y}{2})\Delta_y] \right\} e^{i2\pi n \ell / N_y}. \quad (7)$$

With this formulation, we simply sum along the k_x coordinate followed by a one-dimensional FFT on the k_y coordinate. A similar "one-dimensional collapse" formulation is used to compute the near field along the x -axis.

Near-field computations using this algorithm were tested against both theoretical calculations and experimental data. Thus, in figures 14 and 15 we compare results produced by the planar near-field program against an exact theoretical expression obtained by Rudduck and Chen [19] for the field along the z -axis of a uniform circular aperture. The absolute power densities are obtained by each method and compared in the figures for both a 10λ diameter

circular aperture and a 20λ diameter circular aperture at an operating frequency of 4 GHz. Computed results are plotted as solid lines while theoretical results are plotted as dashed lines. The on-axis electric-field strength for a uniformly excited circular aperture is given by

$$E = \frac{1}{a} \sqrt{\frac{2P_0}{\pi Y_0}} \left(e^{ikz} - \frac{z}{R} e^{ikR} \right); R = \sqrt{z^2 + a^2}$$

where $a = D/2$ is the aperture radius. The close correspondence between computed and theoretical results in these figures is extremely gratifying.

Next, in figures 16 through 21, we show comparisons between computed near-zone results and actual measured data taken at corresponding z-axis distances. The antenna characterized in figures 16 through 18 (antenna #1) has D/λ ratio of 16.2, while the antenna characterized in figures 19 thru 21 (antenna #2) has a D/λ ratio of 77.6. For each antenna, we compare measured data against predicted near fields at the measurement plane and at z-axis distances of 100 cm and 300 cm beyond that. Both antennas are linearly polarized in the y-direction; also, the reconstructed near-fields and the comparison measurements are taken parallel to the y-axis. As seen in the figures, there are fewer reconstructed near-field points than measurements at the shortest distance, due to using a smaller scan area for generating the plane-wave spectrum than for taking comparison measurements. Measured results are plotted as dashed lines while the computed results are plotted as solid lines. Both measured values and computed results are normalized with respect to the corresponding peak field strength in the measurement plane. The agreement shown between measured and computed results is remarkable in view of the very complex pattern structure of these near-zone fields.

Finally, in figures 22 and 23 we show computed near-zone power-density contours in the y-z plane for these same two antennas, while in figure 24 we show theoretical near-zone power-density contours for a 10λ diameter uniformly excited circular aperture at 4 GHz. These contours give absolute power density in dBm/cm² corresponding to one Watt of input power at the antenna aperture.

In conclusion, we have presented an improved algorithm for calculating near-zone fields in the vicinity of radiating aperture or dish antennas and we have demonstrated that our algorithm is capable of extremely high accuracy. We have also presented absolute power-density contours for some of the antennas studied. Such absolute power-density contours are a convenient and informative method for exhibiting near-zone computation results.

Appendix

Here, we wish to obtain integration limits k_{x0} , k_{y0} to bound the oscillatory behaviour of $e^{i\gamma z}$ in the integrand of (4). We do this by making use of the sampling theorem, which requires that there be at least two sample points per cycle at the greatest resolvable "z" spatial frequency. That is, we will only retain those z-component spatial frequencies within the integrand satisfying this criterion, so the maximum allowable incremental change in γ will be π/z . Since $\gamma = \sqrt{k^2 - K^2}$, where $K^2 = k_x^2 + k_y^2$, the applicable criterion for determining the integration domain limits is

$$\frac{\pi}{kz} = \sqrt{1 - (U^2 - b)} - \sqrt{1 - U^2}, \quad (8)$$

where $U \equiv \frac{K_0}{k} = \sqrt{k_{x0}^2 + k_{y0}^2} / k$, and where b represents a small incremental change in U^2 corresponding to a change from the sample point k_{x0} , k_{y0} to the point $k_{x0} - \Delta_x$, $k_{y0} - \Delta_y$. For consistency we require that $k_{x0} + k_{y0} > \Delta_x + \Delta_y$.

The assumption that evanescent modes are negligible in (3) implies that $U < 1$. Accordingly, we can apply the binomial expansion, $\sqrt{1 - U^2} = 1 - \frac{U^2}{2} - \frac{U^4}{8} - \dots$ to (8). After cancelling terms and rearranging series expansions we obtain

$$\frac{\pi}{kz} = \frac{b}{8} \left(1 + \frac{1}{1 - U^2} + \frac{2}{1 - U^2/2} - \frac{U^8}{32} - \frac{5U^{10}}{64} - \dots \right) - 0 \left(\frac{b^2}{8} \right) \quad (9)$$

Neglecting terms of order b^2 or smaller, we can express b as the ratio of a fourth order polynomial to a power series in U^2 . Carrying out the indicated power-series division we obtain

$$b = \frac{2\pi}{kz} \left(1 - \frac{U^2}{2} - \frac{U^4}{8} - \frac{U^6}{16} - \frac{5U^8}{128} - \frac{7U^{10}}{256} - \dots \right) \quad (10)$$

Now let $\Delta \equiv \Delta_x \cong \Delta_y$. Then

$$k^2 b = K_0^2 - (k_{x0} - \Delta)^2 - (k_{y0} - \Delta)^2 = 2\Delta (k_{x0} + k_{y0} - \Delta)$$

$$\text{or } kb = 2\Delta(\alpha U - \frac{\Delta}{k}), \text{ where } \alpha = \cos \phi_0 + \sin \phi_0 ; \phi_0 = \tan^{-1} \frac{k_{y0}}{k_{x0}} .$$

We have (see text following eq. 2) $\Delta = \pi/R_0$, where $R_0 = \frac{1}{2}N_y \delta_y$ is the maximum lateral-coordinate range. Consequently, b^2 in (9) is negligible compared to b provided that $R_0 \gg \lambda$. Now we can express (10) as

$$U^2 + 2 \frac{\alpha z}{R_0} U - \frac{\lambda z}{R_0^2} = 2 - \sigma \quad , \quad (11)$$

where $\sigma = \frac{U^4}{4} + \frac{U^6}{8} + \frac{5U^8}{64} + \dots$. We solve (11) as a simple quadratic equation in U . Then, for $z > R_0$ and neglecting terms smaller than $(\frac{\lambda}{R_0})^2$, we expand the resulting radical as a power series in $\frac{R_0}{\alpha z}$ including the small correction term σ in the expansion. Iteratively substituting into the expression for σ we obtain a corrected series expansion for U , which to an accuracy of $(\frac{R_0}{\alpha z})^{13}$ is equivalent to

$$U = \frac{1}{\sqrt{\left(\frac{\alpha z}{R_0}\right)^2 + 1 + \frac{\lambda z}{R_0^2}}} + \frac{\lambda}{2\alpha R_0} \quad (12)$$

Equation (12)'s greatest source of discrepancy comes from neglecting the b^2 terms in (9), so for z large the discrepancy in U is on the order of $\frac{\lambda R_0}{4\alpha z^2}$. Thus, for $\frac{z}{R_0} > \left(\frac{R_0}{\lambda}\right)^{\frac{1}{2}}$, the discrepancy is less than $\left(\frac{\lambda}{R_0}\right)^2$. From (12) we readily see that our consistency condition, $k_{x0} + k_{y0} > 2\Delta$, is satisfied provided $z < \frac{2R_0^2}{\lambda}$. Finally, neglecting terms of order λ/R_0 , (12) becomes

$$U = \frac{1}{\sqrt{\left(\frac{\alpha z}{R_0}\right)^2 + 1}} .$$

References

- [1] Brown, J., Theoretical analysis of some errors in aerial measurements, Proc. IEE, 105C, 343-351, Feb. 1958.
- [2] Brown, J. and Jull, E.V., The prediction of aerial radiation patterns from near-field measurements, Proc. IEE, 108B, 635-644, Nov. 1961.
- [3] Kerns, D.M., Correction of near-field antenna measurements made with an arbitrary but known measuring antenna, Electronic Letters 6, 346-347, May 1970.
- [4] Newell, A.C. and Kerns, D.M., Determination of both polarization and power gain of antennas by a generalized 3-antenna measurement method, Electronic Letters 7, 68-70, Feb. 1971.
- [5] Kerns, D.M., Plane-wave scattering-matrix theory of antennas and antenna-antenna interactions: formulation and applications, J. Res. NBS-B, 80B, 5-51, Jan.-March 1976.
- [6] Jensen, F., Electromagnetic near-field far-field correlations, PhD dissertation, Tech. Univ. Denmark, Lyngby, 1970.
- [7] Ludwig, A.C., Near-field far-field transformations using spherical-wave expansions, IEEE Trans. Antennas and Propagation, AP-19, 214-220, 1971.
- [8] Johnson, R.C., Ecker, H.A., and Hollis, J.S., Determination of far-field antenna patterns from near-field measurements, IEEE Proceedings 61, 1668-1694, Dec. 1973.
- [9] Leach, W.M. Jr. and Paris, D.T., Probe compensated near-field measurements on a cylinder, IEEE Trans. Antennas and Propagation, AP-21, 435-445, July 1973.
- [10] Kummer, W.H. and Gillespie, E.S., Antenna Measurements - 1978, IEEE Proceedings 66, 483-507, April 1978.

- [11] Newell, A.C., Baird, R.C., and Wacker, P.F., Accurate measurement of antenna gain and polarization at reduced distances by an extrapolation technique, IEEE Trans. Antennas and Propagation, AP-21, 418-431, July 1973.
- [12] Kerns, D.M., Plane-wave scattering-matrix theory of antennas and antenna-antenna interactions, Nat. Bur. Stand. Monograph 162, June 1981.
- [13] Newell, A.C. and Crawford, M.L., Planar near-field measurements on high performance array antennas, Nat. Bur. Stand. Report NBSIR-74-380, July 1974.
- [14] Newell, A.C., Planar near-field measurement techniques, Nat. Bur. Stand. Short Course on Antenna Parameter Measurement by Near-Field techniques lecture notes, July 1975.
- [15] Yaghjian, A.D., Upper-bound errors in far-field antenna parameters determined from planar near-field measurements, Part 1: analysis, Nat. Bur. Stand. Tech. Note 667, Oct. 1975.
- [16] Newell, A.C., Upper-bound errors in far-field antenna parameters determined from planar near-field measurements, Part 2: analysis and computer simulation, Nat. Bur. Stand. Short Course on Antenna Parameter Measurement by Near-Field Techniques lecture notes, July 1975.
- [17] Yaghjian, A.D., Efficient computation of antenna coupling and fields within the near-field region, IEEE Trans. Antennas and Propagation, AP-30, 113-128, Jan. 1982.
- [18] Landu, H.J., Sampling, data transmission, and the Nyquist rate, IEEE Proceedings, 55, 1701-1706, Oct. 1967.
- [19] Rudduck, R.C.; Chen, C.L.J., New plane-wave spectrum formulations for the near field of circular and strip apertures, IEEE Trans. Antennas and Propagation, AP-24, 438-449, July 1976.

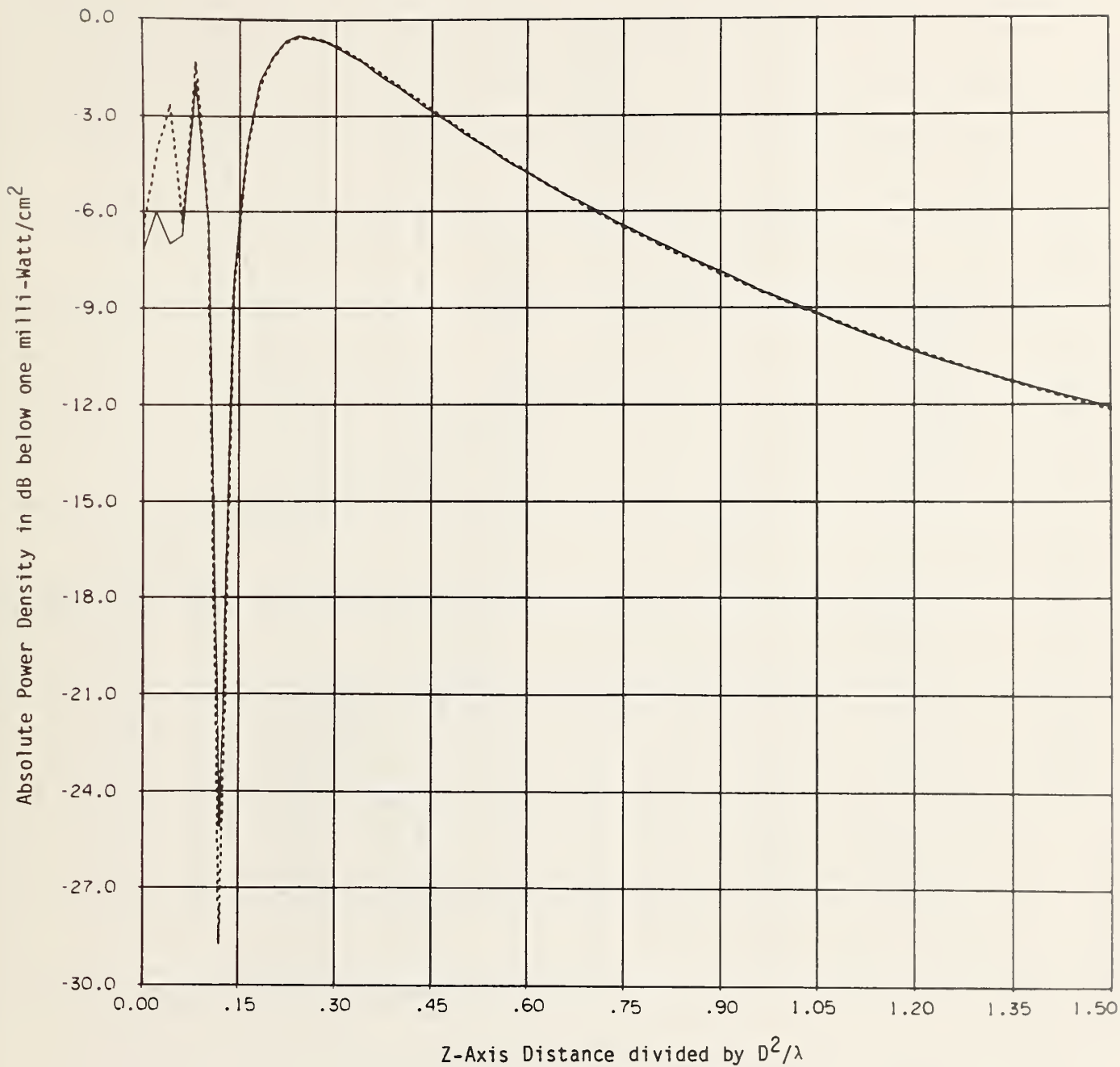


Figure 14. Comparison of results, along the z-axis, as produced by the planar program (solid line) and as calculated using an exact theoretical expression (dashed line) for a $10\text{-}\lambda$ diameter uniformly excited circular aperture at 4 GHz showing power density in dB below one milliwatt/cm², assuming one watt input power to the aperture.

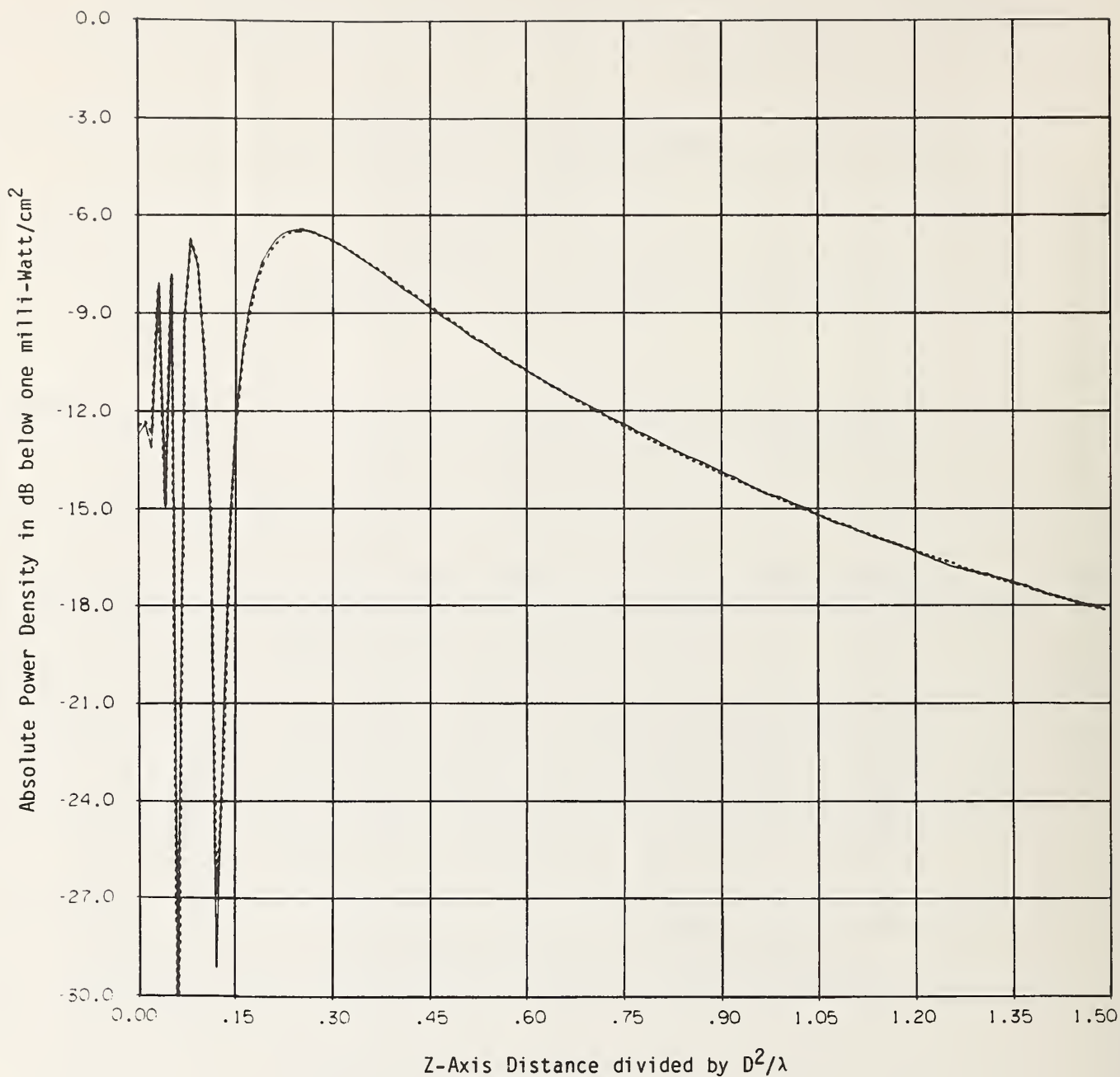


Figure 15. Comparison of results, along the z-axis, as produced by the planar program (solid line) and as calculated using an exact theoretical expression (dashed line) for a $20\text{-}\lambda$ diameter uniformly excited circular aperture at 4 GHz showing power density in dB below one milliwatt/cm², assuming one watt input power to the aperture.

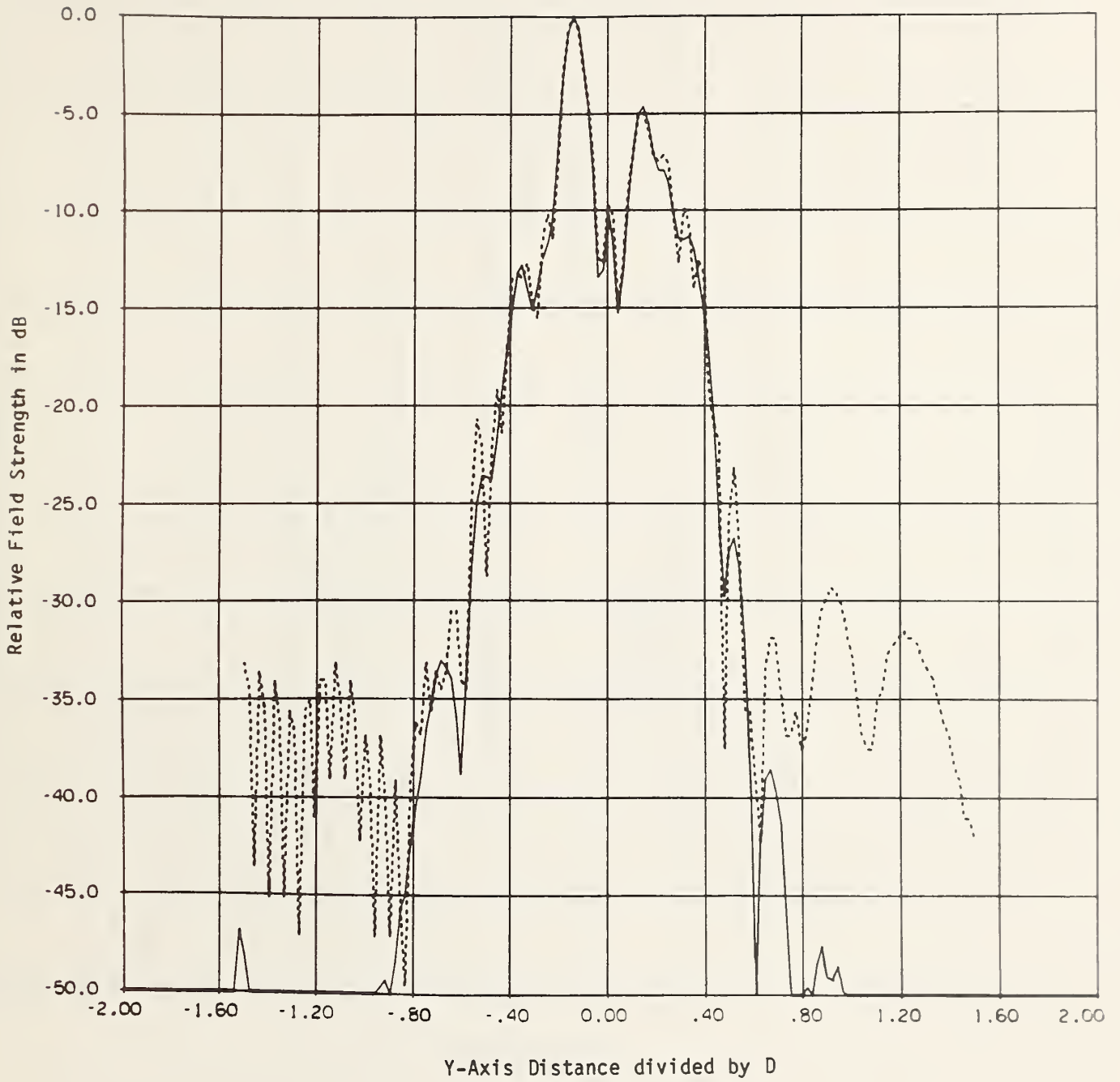


Figure 16. Comparison of Measured (dashed line) and Computed (solid line) Relative E-Plane-Cut Field Intensity Curves for Antenna #1 at $z = 65.3$ cm.

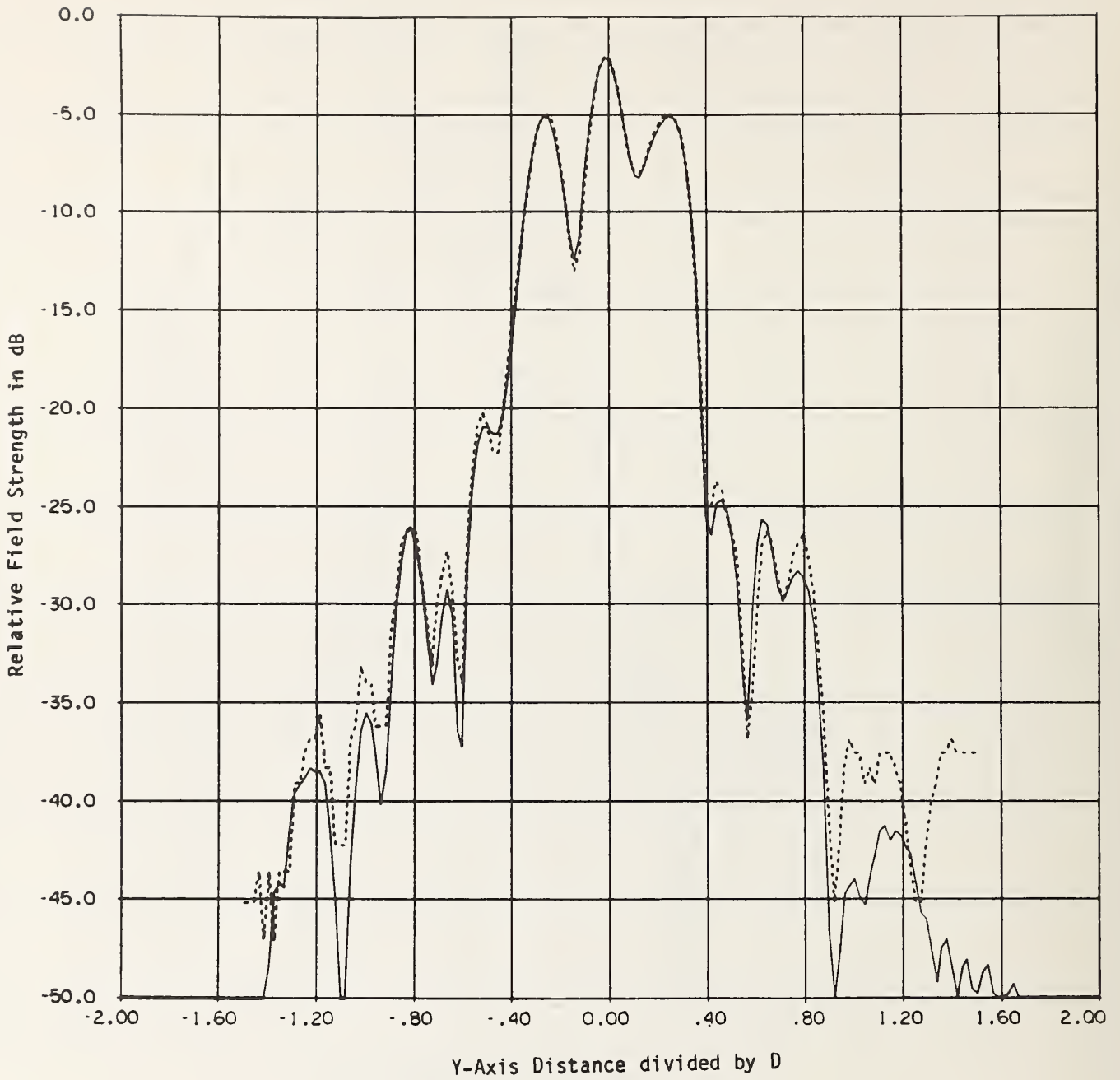


Figure 17. Comparison of Measured (dashed line) and Computed (solid line) Relative E-Plane-Cut Field Intensity Curves for Antenna #1 at $z = 165.3$ cm.

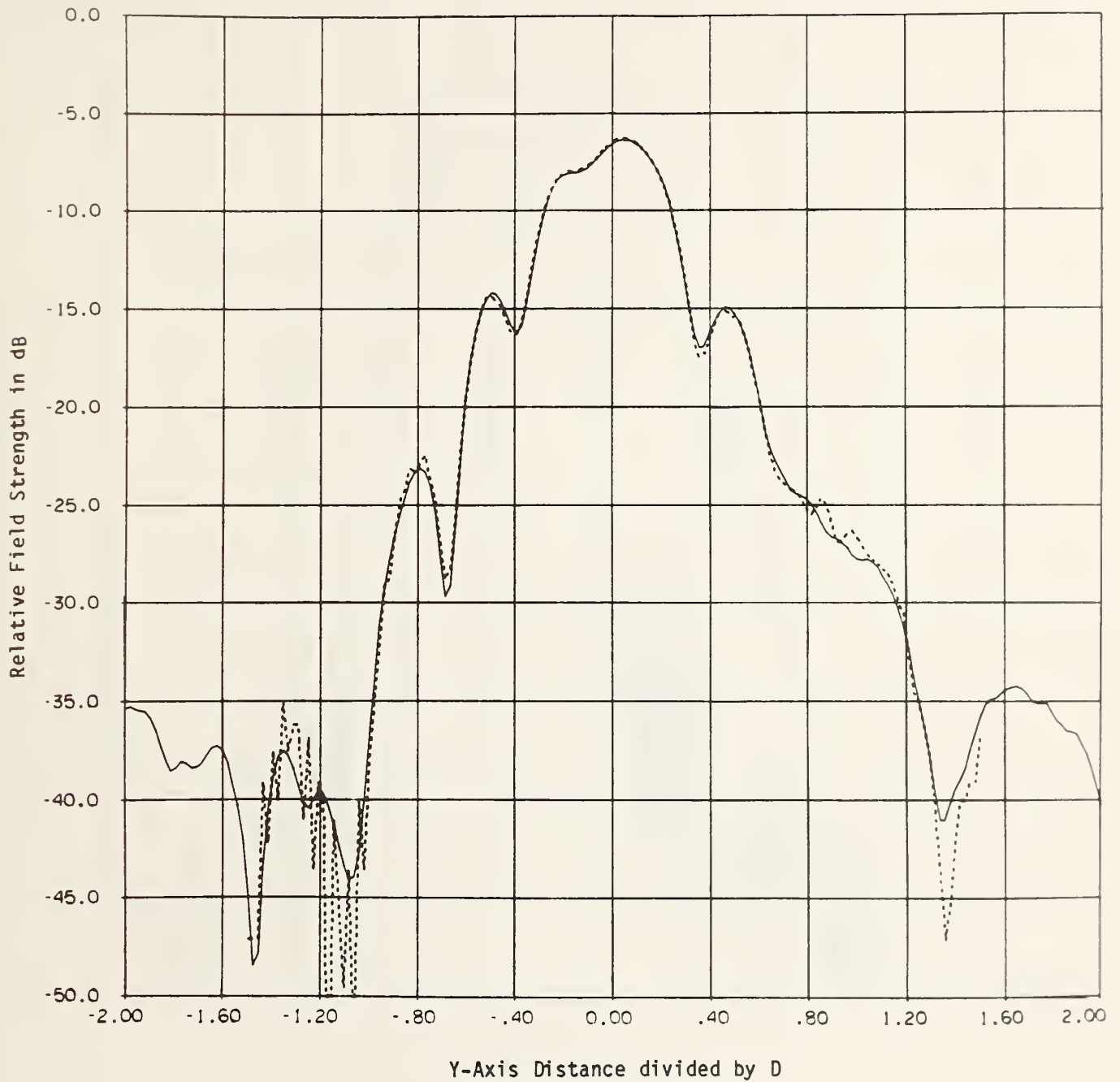


Figure 18. Comparison of Measured (dashed line) and Computed (solid line) Relative E-Plane-Cut Field Intensity Curves for Antenna #1 at $z = 365.3$ cm.

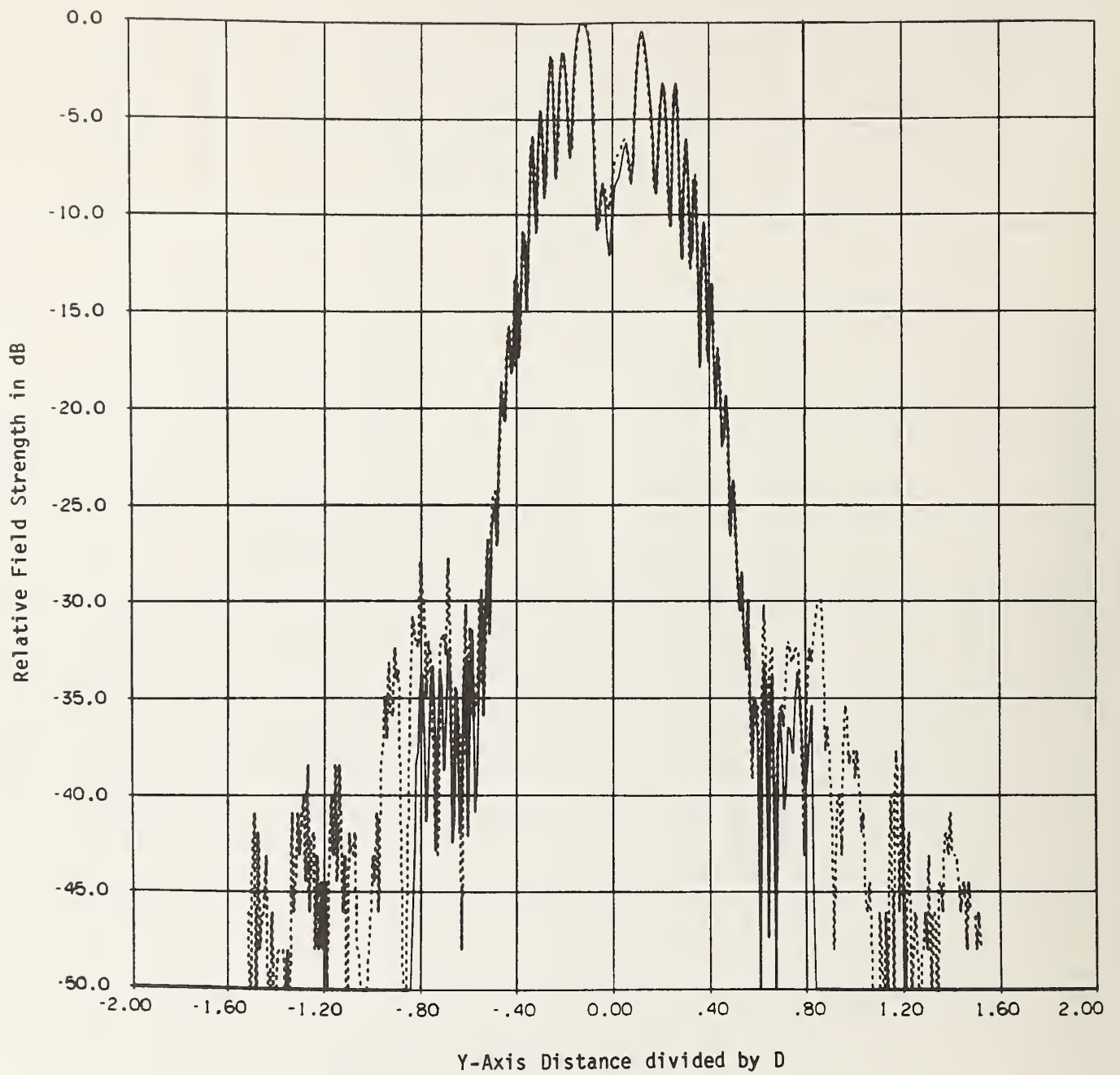


Figure 19. Comparison of Measured (dashed line) and Computed (solid line) Relative E-Plane-Cut Field Intensity Curves for Antenna #2 at $z = 42$ cm.

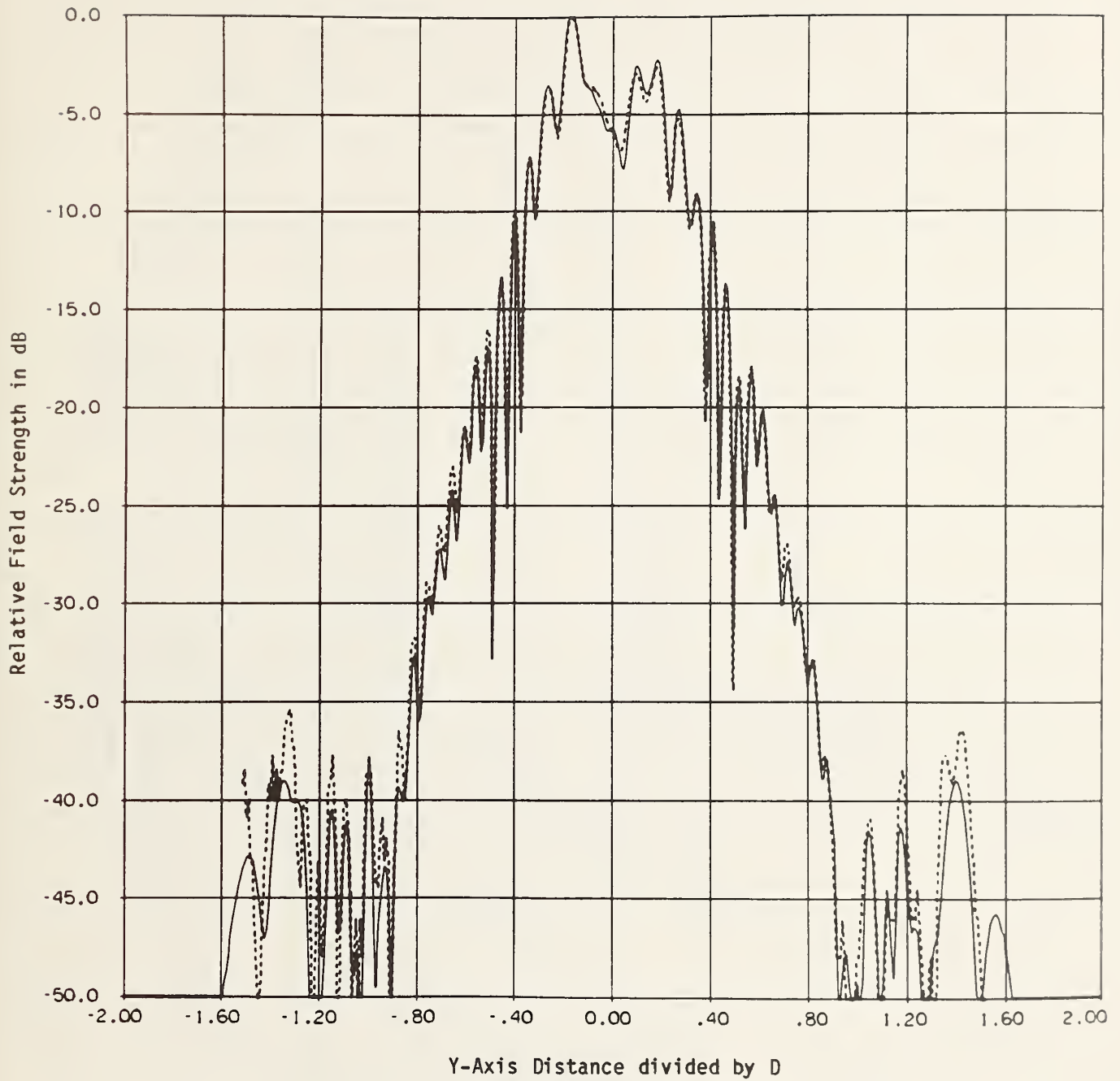


Figure 20. Comparison of Measured (dashed line) and Computed (solid line) Relative E-Plane-Cut Field Intensity Curves for Antenna #2 at $z = 142$ cm.

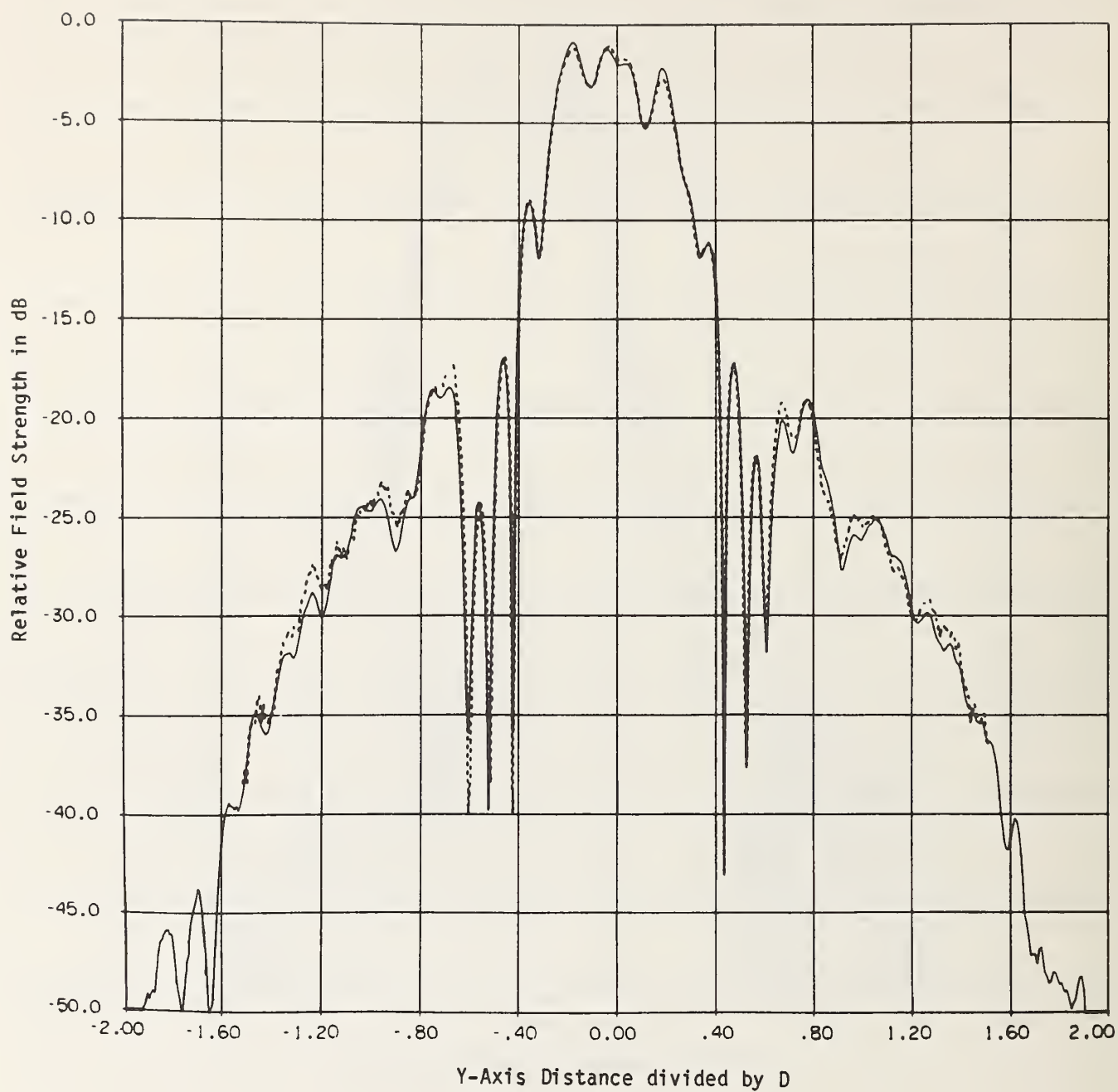


Figure 21. Comparison of Measured (dashed line) and Computed (solid line) Relative E-Plane-Cut Field Intensity Curves for Antenna #2 at $z = 342$ cm.

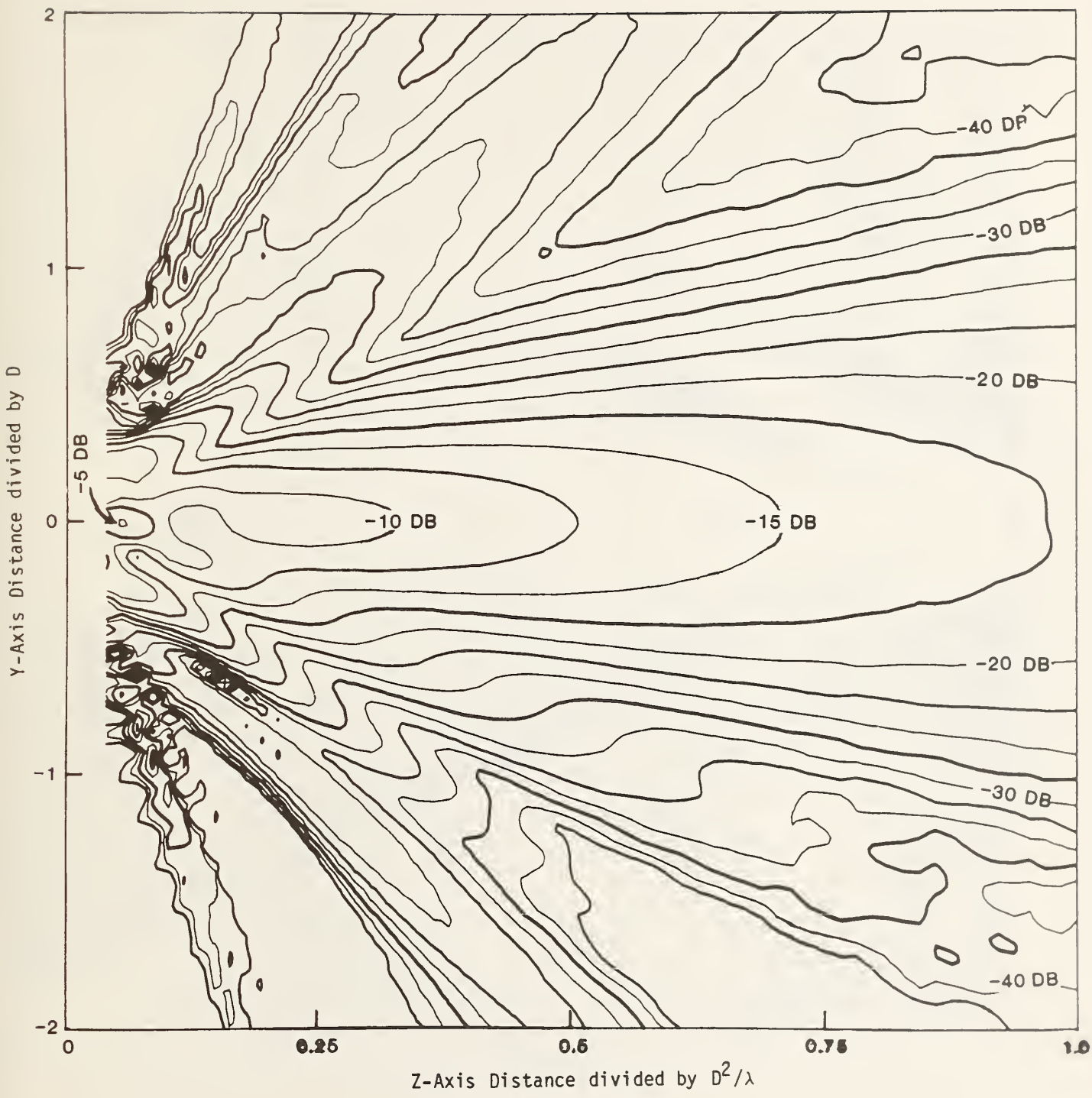


Figure 22. Near-Zone Power Density Contours for Antenna #1 in dB below one milli-Watt/cm² for one Watt input power to the antenna (2.5 dB separation between adjacent contours).

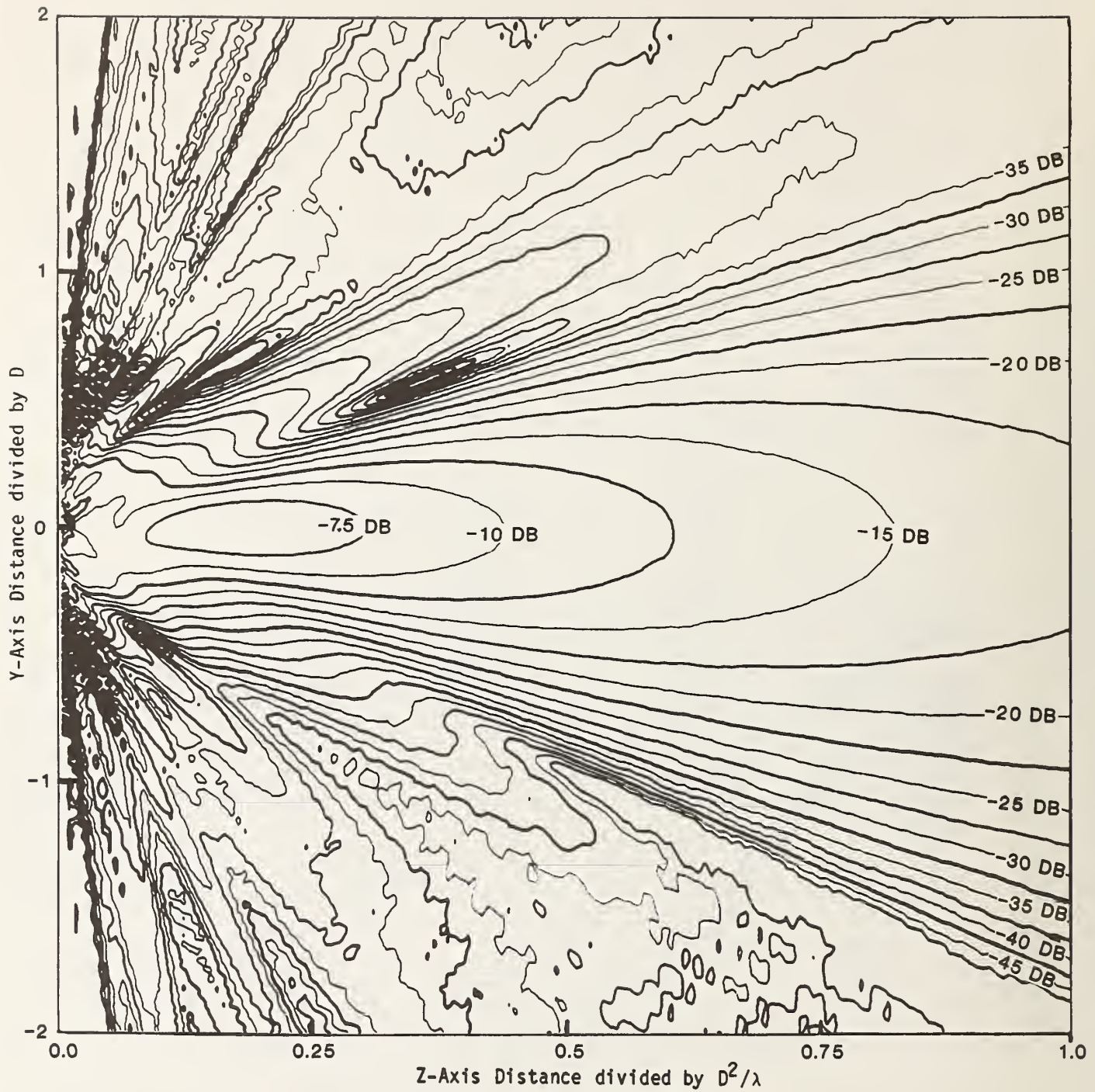


Figure 23. Near-Zone Power Density Contours for Antenna #2 in dB below one milli-Watt/cm² for one Watt input power to the antenna (2.5 dB separation between adjacent contours).

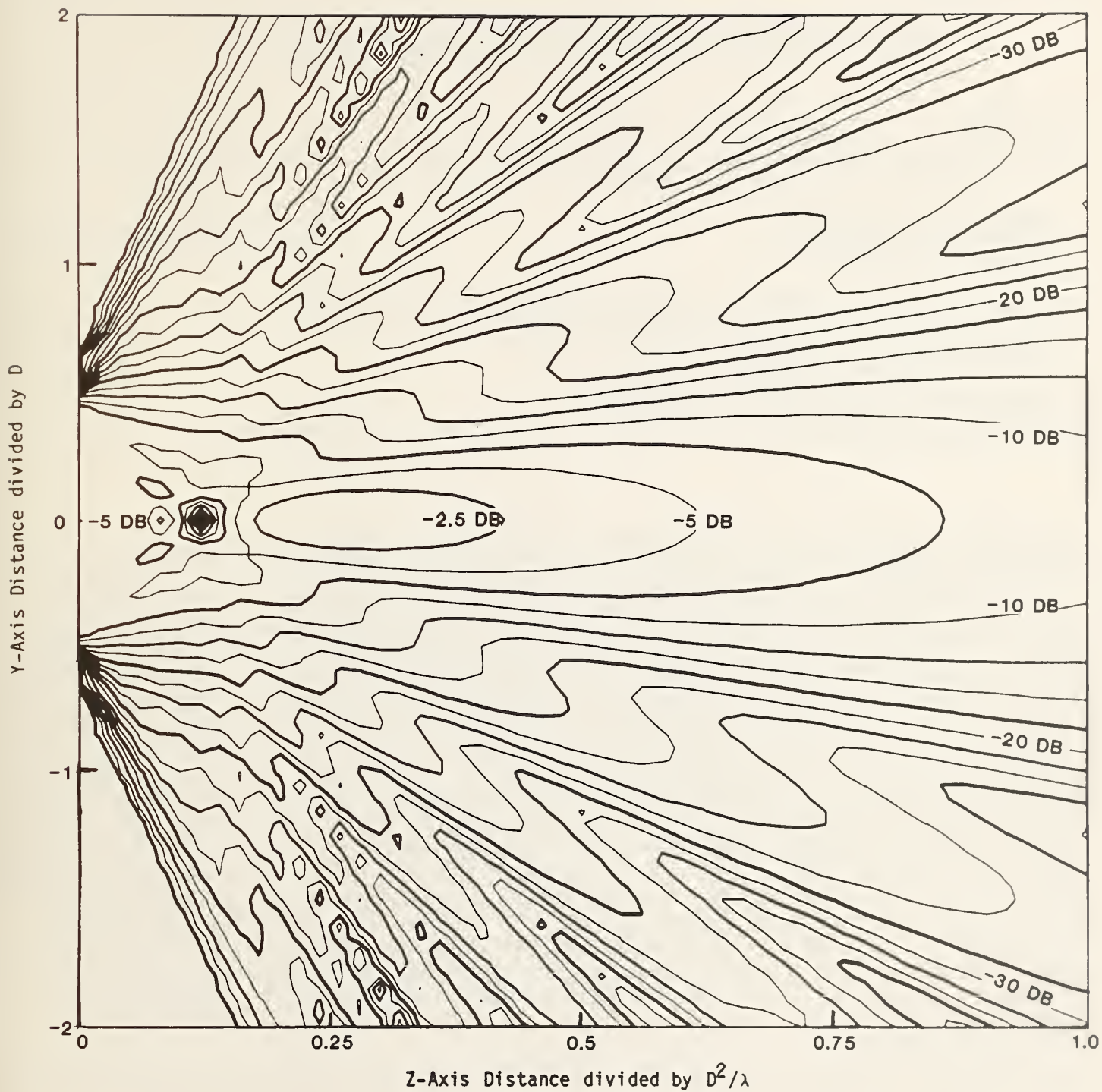


Figure 24. Near-Zone Power Density Contours for a $10\text{-}\lambda$ Diameter Uniformly Excited Circular Aperture in dB below one milli-Watt/cm² at 4 GHz for one Watt input power at the aperture (2.5 dB separation between adjacent contours.)

U.S. DEPT. OF COMM. BIBLIOGRAPHIC DATA SHEET <i>(See instructions)</i>	1. PUBLICATION OR REPORT NO. NBSIR 85-3036	2. Performing Organ. Report No.	3. Publication Date December 1985
4. TITLE AND SUBTITLE <p style="text-align: center;">An Efficient and Accurate Method For Calculating and Representing Power Density in the Near-Zone of Microwave Antennas</p>			
5. AUTHOR(S) Richard L. Lewis & Allen C. Newell			
6. PERFORMING ORGANIZATION <i>(If joint or other than NBS, see instructions)</i> NATIONAL BUREAU OF STANDARDS DEPARTMENT OF COMMERCE WASHINGTON, D.C. 20234		7. Contract/Grant No.	8. Type of Report & Period Covered
9. SPONSORING ORGANIZATION NAME AND COMPLETE ADDRESS <i>(Street, City, State, ZIP)</i> United States Environmental Protection Agency Office of Radiation Programs Analysis and Support Division (ANR-461) Crystal Mall 2, Washington DC 20460			
10. SUPPLEMENTARY NOTES <input type="checkbox"/> Document describes a computer program; SF-185, FIPS Software Summary, is attached.			
11. ABSTRACT <i>(A 200-word or less factual summary of most significant information. If document includes a significant bibliography or literature survey, mention it here)</i> <p>An algorithm is presented for calculating near-zone and Fresnel-region fields in front of microwave antennas from discrete numerical values of the radiated plane-wave spectrum (complex far-field pattern). That is, the near fields are calculated by numerically integrating the plane-wave spectrum representation of the field. The crux of the analysis consists of handling a numerical instability which arises from integrating discrete data. A criterion is developed for limiting the integration domain in order to exclude highly oscillatory regions of the integrand. In turn, this leads to restricting the applicable output range over which the field can be computed. With the numerical instability problem thus resolved, fast Fourier transform techniques are used to assure efficient numerical integration over a large (but restricted) output range. The results are conveniently presented as relative power-density contours in planes formed by the longitudinal coordinate axis and one transverse coordinate axis. The algorithm is capable of extremely high accuracy, which is demonstrated by comparing predicted and measured near fields for two distinct antennas, along with a comparison against an exact theoretical model. In the case of circularly-symmetric excitation models for electrically large antenna apertures, the predicted relative near-zone power-density contour plots turn out to be a function of just the relative aperture distribution. Nomographs for obtaining absolute near-zone power densities are presented for a few typical aperture-distribution functions.</p>			
12. KEY WORDS <i>(Six to twelve entries; alphabetical order; capitalize only proper names; and separate key words by semicolons)</i> antennas; antenna apertures; near fields; Fresnel region; plane-wave spectrum.			
13. AVAILABILITY <input checked="" type="checkbox"/> Unlimited <input type="checkbox"/> For Official Distribution. Do Not Release to NTIS <input type="checkbox"/> Order From Superintendent of Documents, U.S. Government Printing Office, Washington, D.C. 20402. <input checked="" type="checkbox"/> Order From National Technical Information Service (NTIS), Springfield, VA. 22161		14. NO. OF PRINTED PAGES 44	15. Price

